

A Systemic Study of 14 Southern Infrared Dark Clouds with the N_2H^+ , HNC, HCO^+ , and HCN Lines

Xiao-Lan Liu^{1,3*}, Jun-Jie Wang^{1,2} and Jin-Long Xu^{1,2}

¹National Astronomical Observatories, Chinese Academy of Science, Beijing 100012, China

²NAOC-TU Joint Center for Astrophysics, Lhasa 850000, China

³Graduate University of Chinese Academy of Sciences, Beijing, 100049, China

Accepted 1988 December 15. Received 1988 December 14; in original form 1988 October 11

ABSTRACT

We have studied 14 southern infrared dark clouds (*IRDCs*) using the data taken from the *Millimetre Astronomy Legacy Team 90 GHz (MALT90)* survey and the *GLIMPSE* and *MIPSGAL* mid-infrared survey of the inner Galaxy. The physical and chemical characteristics of the 14 *IRDCs* are investigated using N_2H^+ (1-0), HNC(1-0), HCO^+ (1-0), and HCN(1-0) molecular lines. We find that the 14 *IRDCs* are in different evolutionary stages from the “starless” to the sources with an UCHII region. Three *IRDCs* are detected to have the star forming activities. The integrated intensity ratios $I_{\text{HCO}^+/\text{HCN}}$, $I_{\text{N}_2\text{H}^+/\text{HCN}}$, and $I_{\text{HNC}/\text{HCN}}$ are all about 1.5, which is different from the previous measurements, suggesting that the integrated intensity ratios may be affected by the cloud environments. The integrated intensities of HNC, HCO^+ and HCN show a tight correlation for the 14 *IRDCs*, implying a close link to the chemical evolution of these three species in the *IRDCs*. The derived excitation temperature for each *IRDC* is less than 25 K. We estimate the abundances of the four molecules from 10^{-11} to 10^{-9} , and the average abundance ratios $N_{\text{HNC}}/N_{\text{HCN}} = 1.47 \pm 0.50$, $N_{\text{HNC}}/N_{\text{HCO}^+} = 1.74 \pm 0.22$, $N_{\text{HCN}}/N_{\text{HCO}^+} = 1.21 \pm 0.41$.

Key words: astrochemistry; abundances — ISM: *IRDCs* — ISM: clouds — stars: formation — ISM: molecules-ratio lines

1 INTRODUCTION

Infrared dark clouds (*IRDCs*) are the dark extinction regions of high contrast against the bright Galactic mid-infrared background, discovered by the *Midcourse Space Experiment (MSX)* (Carey et al. 1998; Egan et al. 1998) and *infrared Space Observatory (ISO)* surveys (Perault et al. 1996). Simon et al. (2006) identified 10,931 *IRDCs* candidates using *MSX* $8.3\ \mu\text{m}$ data. Jackson et al. (2008) showed that these identified *IRDCs* are located in the fourth quadrant and first quadrant of the Galaxy at a galactocentric distances of 6 kpc and 5 kpc, respectively. Additionally, Peretto & Fuller (2009) identified 11,303 *IRDCs* candidates using *Spitzer* $8\ \mu\text{m}$ data.

Previous researchers suggested that *IRDCs* were the cold ($T < 25\ \text{K}$) and dense ($10^5\ \text{cm}^{-3}$) regions, with a scale of $1\sim 10\ \text{pc}$ and a mass of $10^2 \sim 10^5\ M_\odot$ (Egan et al. 1998; Carey et al. 1998, 2000; Rathborne et al. 2006). Chambers et al. (2009) proposed that the cores within the *IRDCs* may be in different phase, from a quiescent to an active, and finally into a red core. The quiescent cores represent the earliest preprotostellar (starless) core phase without infrared signatures, while the active cores have the extended and enhanced $4.5\ \mu\text{m}$ emission with an embedded $24\ \mu\text{m}$ emission source. When a core shows the polycyclic aromatic hy-

drocarbon (PAH) emission at $8\ \mu\text{m}$, it is considered to be in the finally red core stage. Furthermore, these detected cores have the strong dust emission from millimetre and submillimetre bands (Lis & Carlstrom 1994; Carey et al. 2000; Redman et al. 2003; Rathborne et al. 2005; Beuther et al. 2005; Rathborne et al. 2005, 2006) and only some cores have embedded protostars, indicating that the *IRDCs* may represent the earliest observable stage of high-mass star formation. Thus, *IRDCs* can provide us with an opportunity to study the physical and chemical conditions of massive star-forming processes in the earliest stage.

In this paper, we have analyzed 14 southern *IRDCs* using N_2H^+ (1-0), HNC(1-0), HCO^+ (1-0), and HCN(1-0) molecular lines from the *Millimetre Astronomy Legacy Team 90 GHz (MALT90)* survey (Foster et al. 2011). N_2H^+ , HNC, HCO^+ , and HCN are good tracers of dense gases. And N_2H^+ is known to be a good tracer of the compact center of the cores. Observations of the molecular lines could provide valuable information on the physical and chemical significance of *IRDCs*.

2 DATA

2.1 *IRDCs* selection

Simon et al. (2006) made a $8.3\ \mu\text{m}$ *MSX* *IRDC* catalog containing

* E-mail: liuxiaolan10@mails.gucas.ac.cn

10,931 *IRDC* candidates. Combined this catalog with the *MALT90* survey, we select 18 southern *IRDC* candidates, but only 14 of them have $\text{N}_2\text{H}^+(1-0)$, $\text{HNC}(1-0)$, $\text{HCO}^+(1-0)$, and $\text{HCN}(1-0)$ emission with high signal-noise ratio. These lines are all good tracers of dense gases, but provide slightly different information. N_2H^+ was more resistant to freeze-out on grains than the carbon-bearing species (Bergin et al. 2001). HNC was particularly prevalent in cold gas (Hirota et al. 1998). HCO^+ often showed infall signatures and outflow wings (Rawlings et al. 2004; Fuller et al. 2005). The *Spitzer IRAC* $8\mu\text{m}$ data of these selected *IRDCs* are presented (gray) in Figures 1-14, and the basic information are summarized in Tables 1-2.

2.2 *IRDCs* observations

The data extracted from the *Millimetre Astronomy Legacy Team 90 GHz (MALT90)*, *GLIMPSE* and *MIPSGAL* surveys are analyzed toward the 14 southern *IRDCs*.

MALT90 is a large international project aimed at characterizing high-mass dense cores in the southern sky at 90 GHz with the Mopra 22-m Telescope. The angular resolution of Mopra Telescope is about $38''$. The correction for the line intensities to the main beam brightness temperature scale is made by using the formula $T_{\text{mb}} = T_{\text{A}}^*/\eta_{\nu}$, where η_{ν} is the frequency-dependent beam efficiency. The main beam efficiency at 86 GHz is $\eta_{86\text{GHz}} = 0.49$, and at 110 GHz is $\eta_{110\text{GHz}} = 0.44$ (Lo et al. 2009; Ladd et al. 2005). *MALT90* data cubes are downloaded from online archive¹. The data are reduced by the software CLASS (Continuum and Line Analysis Single-Disk Software) and GREG (Grenoble Graphic).

GLIMPSE is a mid-infrared survey of the inner Galaxy performed with the *Spitzer Space Telescope*. *MIPSGAL* is a survey of the same region as *GLIMPSE*, using the *MIPS* instrument ($24\mu\text{m}$ and $70\mu\text{m}$) on *Spitzer*. We use the mosaicked images of *GLIMPSE* at *Spitzer IRAC* $8\mu\text{m}$ and *MIPSGAL* at $24\mu\text{m}$. *Spitzer IRAC* $8\mu\text{m}$ has an angular resolution between $1.5''$ and $1.9''$ (Fazio et al. 2004; Werner et al. 2004), and the angular resolution of *MIPSGAL* $24\mu\text{m}$ is $\sim 6''$.

3 RESULTS

3.1 Spectra

Figures 1-14 show the average spectra of $\text{N}_2\text{H}^+(1-0)$, $\text{HNC}(1-0)$, $\text{HCO}^+(1-0)$, and $\text{HCN}(1-0)$ of the 14 southern *IRDCs*, respectively. From each Figure, we see that the N_2H^+ and HCN lines present the hyperfine structure (HFS), and their velocity components blend with each other. However, the main velocity component ($1_{23}-0_{12}$) of N_2H^+ is detected clearly for most of the *IRDCs*. The N_2H^+ and HCN lines are fitted using a HFS fit procedure. The fitting results are presented in Table 1. From Table 1, we can find that the optical depths of the N_2H^+ lines are less than 1 for all the *IRDCs*, indicating that the N_2H^+ line is optically thin in the *IRDCs*, which agrees with the previous researches. For the HCN line, it is also optically thin, which is inconsistent with the previous studies. Considering the quality of the HCN lines' data and the unsatisfied HFS fits of the HCN lines, it is probable that we underestimate the optical depths of the HCN lines. The velocity widths of the N_2H^+ lines are between 1 and 3.2. Calculating the velocity dispersion ΔV of the optically thin N_2H^+ line causing by thermal motions:

$$\Delta V_{\text{ther}} = \sqrt{8 \ln 2 kT \left(\frac{1}{m_{\text{obs}}} + \frac{1}{\langle m \rangle} \right)} \quad (1)$$

where T is the gas kinematic temperature, m_{obs} is the mass of the observed species (29 per amu for N_2H^+), and $\langle m \rangle$ is the mean molecular mass (2.3 per amu). For gas with $T = 20\text{ K}$, all the sources have N_2H^+ line widths $\Delta V > \Delta V_{\text{ther}} \approx 0.68$, i.e., having greater nonthermal rather than thermal motions. We assume that the nonthermal motions in the N_2H^+ line width may arise from turbulence (Mardones et al. 1997).

In Figures 1-14, the HNC and HCO^+ spectra show a wide variety of line profiles including the double peak, a peak and a "shoulder", a peak skewed to the blue side and single symmetric lines. The HNC and HCO^+ line shapes differ from source to source but are usually similar to each other. The N_2H^+ line, on the other hand, is Gauss toward almost all the sources. In sources with symmetric HNC and HCO^+ lines, their peak velocity lies very close to that of the N_2H^+ line. In sources with double-peaked HNC and HCO^+ lines, the N_2H^+ peak velocity lies between the two peaks (or between the peak and the shoulder), indicating that the complex HNC and HCO^+ line profiles arise from self-absorption at low velocities. The Gauss fit is used for the HNC and HCO^+ lines and the fitting results are listed in Table 2.

$\text{N}_2\text{H}^+(1-0)$, $\text{HNC}(1-0)$, $\text{HCO}^+(1-0)$, and $\text{HCN}(1-0)$ all have much higher critical density ($\geq 10^5\text{ cm}^{-3}$) for collisional excitation. Therefore, there are no other $\text{N}_2\text{H}^+(1-0)$, $\text{HNC}(1-0)$, $\text{HCO}^+(1-0)$, and $\text{HCN}(1-0)$ sources in the line of sight direction. For this reason, we can use the V_{LSR} of the molecules to determine the kinematic distance to each *IRDC*, according to the rotation curve of Reid et al. (2009), where the Galactic center is $R_0 = 8.4 \pm 0.6\text{ kpc}$ and a circular rotation speed is $Q_0 = 254 \pm 16\text{ km s}^{-1}$. Therefore, four far and four near kinematic distances are obtained for each *IRDC*. The calculating results are in Tables 1-2. Since *IRDCs* are perceived as dark extinction features against the Galactic background, it is reasonable to assume that all *IRDCs* are located at the near kinematic distances. Under this assumption, we can obtain the average kinematic distance and its corresponding error from the four molecules for every *IRDC*. Here, we do not consider the errors resulting from the uncertainties of positions and the rotation curve. The final results are listed in Table 3.

3.2 The mm and infrared emission in the *IRDCs*

Figures 1-14 show also the diagrams of N_2H^+ , HNC , HCO^+ and HCN integrated intensity superimposing on the *Spitzer IRAC* $8\mu\text{m}$ and *MIPSGAL* $24\mu\text{m}$ emission images for every *IRDC*. The integrated intensities are calculated for each line in the same velocity range presented in Tables 1-2 for each *IRDC*. Comparing the IR emission of each *IRDC*, 14 *IRDCs* may be divided into different evolutionary stages, from the "starless" to the sources with strong $8\mu\text{m}$ emission. From Figures 1-14, we find that the HNC and N_2H^+ emission both match the silhouettes of *IRDCs* presented by $8\mu\text{m}$ extinction. Hence, HNC and N_2H^+ molecules can be used to study the morphology of *IRDCs* in different stages.

IRDC G003.399-00.399 - In Figure 1, the emission of N_2H^+ and HNC lines show a similar morphology with a single core, but which are different from that of HCO^+ and HCN . There are $24\mu\text{m}$ and $8\mu\text{m}$ emission sources close to the peak of N_2H^+ emission.

IRDC G003.436-00.572 - In Figure 2, the integrated intensity maps of $\text{N}_2\text{H}^+(1-0)$, $\text{HNC}(1-0)$, $\text{HCO}^+(1-0)$, and $\text{HCN}(1-0)$ lines all show a morphology extended from south-east to north-

¹ <http://atoa.atnf.csiro.au/MALT90/>

Table 1. The physical parameters for molecular lines N_2H^+ and HCN. And all the parameters are averaged on the pixels with the integrated intensity $> 5\sigma$ and the intensity $> 3\sigma$.

source	l deg	b deg	molecular line	T_{ex} K	V_{LSR} (km s^{-1})	Width (km s^{-1})	τ	$\int T_{\text{mb}} dv$ ($\text{K} \cdot \text{km s}^{-1}$)	Integrated range (km s^{-1})	d_{far} kpc	d_{near} kpc
G003.399-00.399	3.310	-0.398	N_2H^+	19.81 ± 1.62	6.36 ± 0.18	2.57 ± 0.36	0.11 ± 0.12	5.21 ± 0.30	(2.9)	14.22	2.55
	3.310	-0.398	HCN	17.71 ± 1.50	6.22 ± 0.28	2.09 ± 0.55	0.13 ± 0.13	2.41 ± 0.30	(2.9)	14.26	2.51
G003.436-00.572	3.437	-0.571	N_2H^+	12.05 ± 1.27	2.67 ± 0.12	1.33 ± 0.28	0.16 ± 0.20	2.84 ± 0.21	(0.5)	15.51	1.26
	3.437	-0.571	HCN	16.28 ± 1.24	2.36 ± 0.34	2.28 ± 0.61	0.11 ± 0.59	1.72 ± 0.22	(0.5)	15.64	1.13
G010.402-00.202	10.403	-0.202	N_2H^+	17.22 ± 1.13	11.70 ± 0.13	1.71 ± 0.29	0.12 ± 0.10	3.84 ± 0.20	(8.5,14.5)	14.78	1.74
	10.403	-0.202	HCN	14.23 ± 1.24	11.32 ± 0.41	3.09 ± 0.72	0.12 ± 0.62	2.28 ± 0.23	(8.5,14.5)	14.83	1.70
G010.990-00.083	10.990	-0.082	N_2H^+	12.76 ± 1.04	29.42 ± 0.12	1.96 ± 0.28	0.15 ± 0.14	3.74 ± 0.19	(26.32)	13.22	3.27
	10.990	-0.082	HCN	14.74 ± 1.03	28.90 ± 0.32	2.14 ± 0.63	0.10 ± 0.68	1.31 ± 0.19	(26.32)	13.26	3.24
G308.121-00.152	308.122	-0.336	N_2H^+	14.55 ± 1.17	-47.17 ± 0.17	1.67 ± 0.36	0.11 ± 0.15	2.46 ± 0.21	(-50,-44)	6.71	3.63
	308.122	-0.336	HCN	18.91 ± 1.07	-47.21 ± 0.24	2.21 ± 0.50	0.11 ± 0.48	2.03 ± 0.20	(-50,-44)	6.70	3.63
G317.701+00.110	317.701	+0.110	N_2H^+	15.65 ± 1.40	-43.59 ± 0.13	1.96 ± 0.31	0.15 ± 0.15	3.53 ± 0.21	(-44,-40)	9.76	2.63
	317.701	+0.110	HCN	14.53 ± 1.46	-42.03 ± 0.33	1.89 ± 0.51	0.13 ± 0.65	1.34 ± 0.24	(-44,-40)	9.85	2.54
G321.756+00.029	321.756	+0.030	N_2H^+	15.23 ± 1.26	-32.22 ± 0.12	1.47 ± 0.29	0.14 ± 0.16	3.55 ± 0.22	(-35,-29)	11.21	1.95
	321.756	+0.030	HCN	12.95 ± 1.25	-32.50 ± 0.25	2.43 ± 0.54	0.17 ± 0.43	2.76 ± 0.23	(-35,-29)	11.20	1.97
G331.035-00.418	331.035	-0.418	N_2H^+	18.94 ± 1.22	-64.44 ± 0.17	2.72 ± 0.33	0.11 ± 0.06	6.08 ± 0.28	(-70,-60)	11.05	3.63
	331.035	-0.418	HCN	7.41 ± 1.14	-65.13 ± 0.31	4.16 ± 0.59	0.38 ± 0.26	8.11 ± 0.30	(-70,-60)	11.02	3.66
G331.708+00.583	331.708	+0.584	N_2H^+	23.32 ± 1.17	-67.46 ± 0.15	3.18 ± 0.28	0.11 ± 0.06	10.69 ± 0.27	(-71,-61)	11.00	3.77
	331.708	+0.584	HCN	6.94 ± 1.14	-68.09 ± 0.33	2.98 ± 0.61	0.31 ± 0.71	3.60 ± 0.26	(-71,-61)	10.97	3.80
G334.198-00.202	334.199	-0.201	N_2H^+	12.65 ± 1.04	-48.03 ± 0.15	1.84 ± 0.38	0.13 ± 0.15	3.02 ± 0.20	(-51,-44)	12.12	2.98
	334.199	-0.201	HCN	13.68 ± 1.03	-49.20 ± 0.36	2.00 ± 0.60	0.10 ± 0.75	1.37 ± 0.20	(-51,-44)	12.07	3.04
G337.764-00.338	337.765	-0.337	N_2H^+	20.69 ± 1.12	-41.77 ± 0.12	1.92 ± 0.26	0.11 ± 0.07	4.89 ± 0.21	(-45,-38)	12.68	2.85
	337.765	-0.337	HCN	14.53 ± 1.07	-42.46 ± 0.23	1.98 ± 0.50	0.13 ± 0.30	2.06 ± 0.21	(-45,-38)	12.65	2.88
G341.942-00.167	341.944	-0.166	N_2H^+	22.44 ± 1.35	-42.40 ± 0.15	2.77 ± 0.29	0.11 ± 0.07	8.40 ± 0.31	(-47,-37)	12.78	3.17
	341.944	-0.166	HCN	12.36 ± 1.38	-44.01 ± 0.28	3.37 ± 0.55	0.22 ± 0.37	6.88 ± 0.33	(-47,-37)	12.70	3.25
G344.726-00.541	344.727	-0.540	N_2H^+	10.82 ± 1.14	-33.15 ± 0.14	1.29 ± 0.33	0.15 ± 0.33	2.04 ± 0.18	(-36,-31.5)	13.27	2.92
	344.727	-0.540	HCN	15.79 ± 1.07	-33.13 ± 0.29	1.74 ± 0.58	0.10 ± 0.68	1.08 ± 0.18	(-36,-31.5)	13.27	2.92
G345.556+00.026	345.557	-0.055	N_2H^+	13.03 ± 1.18	-16.63 ± 0.11	1.07 ± 0.27	0.14 ± 0.38	1.92 ± 0.19	(-19,-14)	14.48	1.78
	345.557	-0.055	HCN	15.40 ± 1.16	-16.64 ± 0.32	2.08 ± 0.56	0.11 ± 0.52	1.54 ± 0.20	(-19,-14)	14.45	1.81

Table 2. The physical parameters for molecular lines HNC and HCO^+ . And all the parameters are averaged on the pixels with the integrated intensity $> 5\sigma$ and the intensity $> 3\sigma$.

source	l deg	b deg	molecular lines	T_{mb} K	V_{LSR} (km s^{-1})	Width (km s^{-1})	τ	$\int T_{\text{mb}} dv$ ($\text{K} \cdot \text{km s}^{-1}$)	Integrated range (km s^{-1})	d_{far} kpc	d_{near} kpc
G003.399-00.399	3.310	-0.398	HNC	1.37 ± 0.34	6.13 ± 0.20	2.80 ± 0.53	0.10 ± 0.03	4.11 ± 0.29	(2.9)	14.29	2.48
	3.310	-0.398	HCO^+	1.33 ± 0.35	6.34 ± 0.18	1.89 ± 0.45	0.10 ± 0.03	3.09 ± 0.30	(2.9)	14.23	2.54
G003.436-00.572	3.437	-0.571	HNC	1.22 ± 0.28	2.52 ± 0.17	1.10 ± 0.42	0.10 ± 0.02	2.71 ± 0.21	(0.5)	15.57	1.20
	3.437	-0.571	HCO^+	1.06 ± 0.28	1.58 ± 0.16	1.47 ± 0.41	0.08 ± 0.02	1.73 ± 0.21	(0.5)	15.98	0.79
G010.402-00.202	10.403	-0.202	HNC	1.04 ± 0.25	11.81 ± 0.21	3.31 ± 0.51	0.10 ± 0.03	3.43 ± 0.20	(8.5,14.5)	14.77	1.76
	10.403	-0.202	HCO^+	0.98 ± 0.26	11.93 ± 0.26	4.06 ± 0.61	0.09 ± 0.03	3.90 ± 0.21	(8.5,14.5)	14.75	1.77
G010.990-00.083	10.990	-0.082	HNC	0.96 ± 0.23	28.87 ± 0.22	3.27 ± 0.55	0.09 ± 0.02	3.03 ± 0.18	(26.32)	13.26	3.23
	10.990	-0.082	HCO^+	0.84 ± 0.23	28.08 ± 0.20	2.24 ± 0.53	0.08 ± 0.02	1.97 ± 0.19	(26.32)	13.32	3.18
G308.121-00.152	308.122	-0.336	HNC	1.28 ± 0.25	-47.16 ± 0.16	2.57 ± 0.40	0.08 ± 0.02	3.42 ± 0.20	(-50,-44)	6.71	3.63
	308.122	-0.336	HCO^+	1.60 ± 0.26	-47.49 ± 0.13	2.24 ± 0.32	0.11 ± 0.02	3.99 ± 0.21	(-50,-44)	6.67	3.67
G317.701+00.110	317.701	+0.110	HNC	1.43 ± 0.29	-42.92 ± 0.18	2.65 ± 0.48	0.13 ± 0.03	3.17 ± 0.20	(-44,-40)	9.80	2.59
	317.701	+0.110	HCO^+	1.26 ± 0.30	-42.08 ± 0.20	2.73 ± 0.53	0.12 ± 0.03	3.13 ± 0.20	(-44,-40)	9.85	2.55
G321.756+00.029	321.756	+0.030	HNC	1.48 ± 0.29	-32.27 ± 0.15	2.13 ± 0.34	0.16 ± 0.04	3.52 ± 0.24	(-35,-29)	11.21	1.96
	321.756	+0.030	HCO^+	1.62 ± 0.30	-32.52 ± 0.16	2.53 ± 0.39	0.18 ± 0.04	4.39 ± 0.24	(-35,-29)	11.19	1.97
G331.035-00.418	331.035	-0.418	HNC	1.54 ± 0.26	-64.35 ± 0.19	4.25 ± 0.43	0.44 ± 0.14	6.94 ± 0.27	(-70,-60)	11.05	3.62
	331.035	-0.418	HCO^+	2.29 ± 0.28	-64.32 ± 0.14	4.52 ± 0.33	0.75 ± 0.26	11.11 ± 0.29	(-70,-60)	11.05	3.62
G331.708+00.583	331.708	+0.584	HNC	1.23 ± 0.25	-67.85 ± 0.19	3.23 ± 0.45	0.38 ± 0.15	4.37 ± 0.26	(-71,-61)	10.98	3.79
	331.708	+0.584	HCO^+	1.33 ± 0.26	-68.20 ± 0.18	3.02 ± 0.44	0.42 ± 0.16	4.44 ± 0.27	(-71,-61)	10.97	3.80
G334.198-00.202	334.199	-0.201	HNC	0.92 ± 0.23	-48.16 ± 0.21	2.87 ± 0.54	0.09 ± 0.02	2.82 ± 0.20	(-51,-44)	12.12	2.99
	334.199	-0.201	HCO^+	0.88 ± 0.24	-49.41 ± 0.17	1.58 ± 0.39	0.09 ± 0.03	1.89 ± 0.21	(-51,-44)	12.06	3.05
G337.764-00.338	337.765	-0.337	HNC	1.81 ± 0.26	-41.97 ± 0.12	2.68 ± 0.30	0.17 ± 0.03	5.21 ± 0.23	(-45,-38)	12.67	2.86
	337.765	-0.337	HCO^+	1.39 ± 0.26	-42.72 ± 0.16	2.42 ± 0.38	0.13 ± 0.03	3.42 ± 0.23	(-45,-38)	12.64	2.90
G341.942-00.167	341.944	-0.166	HNC	1.92 ± 0.30	-43.02 ± 0.17	3.99 ± 0.43	0.23 ± 0.04	8.46 ± 0.31	(-47,-37)	12.75	3.20
	341.944	-0.166	HCO^+	2.30 ± 0.32	-43.76 ± 0.16	3.93 ± 0.42	0.29 ± 0.05	10.00 ± 0.33	(-47,-37)	12.72	3.24
G344.726-00.541	344.727	-0.540	HNC	0.99 ± 0.25	-32.95 ± 0.18	2.08 ± 0.40	0.08 ± 0.02	2.11 ± 0.17	(-36,-31.5)	13.28	2.91
	344.727	-0.540	HCO^+	0.94 ± 0.27	-33.32 ± 0.22	2.47 ± 0.55	0.08 ± 0.02	2.18 ± 0.19	(-36,-31.5)	13.26	2.93
G345.556+00.026	345.557	-0.055	HNC	0.96 ± 0.25	-16.61 ± 0.18	1.99 ± 0.42	0.08 ± 0.02	2.01 ± 0.18	(-19,-14)	14.45	1.80
	345.557	-0.055	HCO^+	0.99 ± 0.26	-16.78 ± 0.19	2.16 ± 0.43	0.08 ± 0.02	2.17 ± 0.19	(-19,-14)	14.44	1.82

west. Two compact cores are clearly shown in HCN line emission, but we cannot see the obvious IR emission. This *IRDC* seems to be a "starless".

IRDC G10.402-00.202 and *IRDC* G10.990-00.083 - From Figure 3 and Figure 4, we can see that both *IRDCs* present elongated structures in all the molecular emission, but have different extended directions. For *IRDC* G10.402-00.202, the integrated intensity map of $\text{N}_2\text{H}^+(1-0)$ show two cores. while *IRDC* G10.990-00.083 contains three compact cores. At the same time, the spectral profiles of both *IRDCs* have double peaks in HNC and HCO^+ lines, while the optical thin line $\text{N}_2\text{H}^+(1-0)$ have a single peak. An $24 \mu\text{m}$ emission source is close to the peak of the molecular emission in both *IRDCs*.

IRDC G308.121-00.337 - In the diagrams of Figure 5, a north-east elongated and compact structure is showed in the four molecular emission, which contains two cores. An $8 \mu\text{m}$ emission source is close to the peak of N_2H^+ emission. The spectra of HNC and HCO^+ exhibit the asymmetric profile.

IRDC G317.701+00.110 - A compact core and an extended core are showed in the integrated intensity map of N_2H^+ and HNC lines in Figure 6. At the center of the compact core, there are obvious emission at $24 \mu\text{m}$ and $8 \mu\text{m}$, here we do not detect the emission of the HCN line in this *IRDC*.

IRDC G321.756+00.029 - Figure 7 shows a compact core elongating from SE to NW in the four molecular emission. It

Table 3. The integrated intensity ratios of the four species.

Source	$I_{\text{N}_2\text{H}^+}/\text{HCN}$	$I_{\text{HNC}}/\text{HCN}$	$I_{\text{HCO}^+}/\text{HCN}$	$I_{\text{HCN}}/\text{HCO}^+$	d(kpc)
G003.399-00.399	2.16 ± 0.30	1.71 ± 0.24	1.28 ± 0.20	0.78 ± 0.12	2.52 ± 0.04
G003.436-00.572	1.65 ± 0.24	1.58 ± 0.24	1.01 ± 0.18	0.99 ± 0.18	1.10 ± 0.30
G010.402-00.202	1.68 ± 0.19	1.50 ± 0.18	1.71 ± 0.20	0.58 ± 0.07	1.74 ± 0.04
G010.990-00.083	2.85 ± 0.44	2.31 ± 0.36	1.50 ± 0.26	0.66 ± 0.12	3.23 ± 0.05
G308.121-00.152	1.21 ± 0.16	1.68 ± 0.19	1.97 ± 0.22	0.51 ± 0.06	3.64 ± 0.03
G317.701+00.110	2.63 ± 0.50	2.37 ± 0.45	2.34 ± 0.44	0.43 ± 0.08	2.58 ± 0.05
G321.756+00.029	1.29 ± 0.13	1.28 ± 0.14	1.59 ± 0.16	0.63 ± 0.06	1.96 ± 0.01
G331.035-00.418	0.75 ± 0.04	0.86 ± 0.05	1.37 ± 0.06	0.73 ± 0.03	3.63 ± 0.03
G331.708+00.583	2.97 ± 0.23	1.21 ± 0.11	1.23 ± 0.12	0.81 ± 0.08	3.79 ± 0.02
G334.198-00.202	2.20 ± 0.35	2.06 ± 0.33	1.38 ± 0.25	0.72 ± 0.13	3.02 ± 0.04
G337.764-00.338	2.37 ± 0.26	2.53 ± 0.28	1.66 ± 0.20	0.60 ± 0.07	2.87 ± 0.03
G341.942-00.167	1.22 ± 0.07	1.23 ± 0.07	1.45 ± 0.08	0.69 ± 0.04	3.22 ± 0.05
G344.726-00.541	1.89 ± 0.36	1.95 ± 0.36	2.02 ± 0.38	0.50 ± 0.09	2.92 ± 0.01
G345.556+00.026	1.25 ± 0.20	1.31 ± 0.21	1.41 ± 0.22	0.71 ± 0.11	1.80 ± 0.02

seems that there are no $24\ \mu\text{m}$ and $8\ \mu\text{m}$ emission in the *IRDC* G321.756+00.029.

IRDC G331.035-00.418 - In Figure 8, the morphologies of the four molecular emission all extend from NE to SW. There are only one core and an extend structure showed in the N_2H^+ emission, but several cores are identified in other molecular emission. From IR emission, we find that it is probable a starless source associated with an UCHII region in its southeast (Bronfman et al. 1996). According to the discussion of section 4.1, it may be an infall candidate.

IRDC G331.708+00.583 - The four molecular emission clearly show two cores in this *IRDC* in Figure 9. Cyganowski et al. (2008) identified it as an extended Green Objects (EGO) source and an outflow candidate. Here we detect a double-peaked profile in HNC and HCO^+ lines, implying that it is likely to be an infall candidate.

IRDC G334.198-00.202 - From the diagrams of Figure 10, N_2H^+ emission shows an extended structure associated with the $24\ \mu\text{m}$ and $8\ \mu\text{m}$ emission, while the showed structures are complicated for other molecular emission because of the weak signal-to-noise ratio.

IRDC G337.764-00.338 - In Figure 11, the four molecular emission all show a morphology extending from NE to SW. The integrated intensity map of N_2H^+ line displays a compact core extending toward northeast, while the HNC line emission shows that *IRDC* G337.764-00.338 has two cores. The optically thick HNC and HCO^+ lines present asymmetric profiles.

IRDC G341.942-00.167 - In Figure 12, the four molecular emission show a similar morphology with a single core. Bronfman et al. (1996) suggested that *IRDC* G341.942-00.167 is associated with an UCHII region. We also detect strong $24\ \mu\text{m}$ and $8\ \mu\text{m}$ emission in this cloud. The HNC line profile shows a peak and a shoulder, but that of HCO^+ is double-peaked, which may be caused by an infall motion.

IRDC G344.726-00.541 and *IRDC* G345.556+00.026 - In Figures 13-14, the emission of N_2H^+ , HNC and HCO^+ lines present similar morphology. Seeing the IR emission of them, both of them are starless. For *IRDC* G345.556+00.026, the HCO^+ lines show a absorption dip in the redshift relative to the V_{LSR} .

4 DISCUSSION

4.1 infall and outflow

For self-absorbed optically thick lines, the classical signature of infall is a double-peaked profile with the blueshifted peak being stronger, or a line asymmetry with the peak skewed to the blue side, while optically thin lines should show a single velocity component peaked at the line center. In section 3.2, some *IRDCs* present the blue profiles. In order to provide a strong evidence on whether these sources have the infall motion, we plot the map grids of $\text{HCO}^+(1-0)$ for each *IRDCs* and find only three *IRDCs* (*IRDC* G331.035-00.418, *IRDC* G331.708+00.583 and *IRDC* G341.942-00.167) may have the infall motions. Figures 15-16 show the map grids towards the three *IRDCs*, which seems to show the infall features in the whole mapping observations. However, in order to affirm that the spectra in the mappings really show the infall signatures, we extract the molecular lines from two positions (In Figures 15-16). In every diagram of the spectra, the optically thin N_2H^+ line is plotted in black color, while the optically thick HNC and HCO^+ lines are presented in green and blue, respectively. The black dash lines and the red dash lines mark the positions of the V_{LSR} of N_2H^+ line and the absorption dip of optically thick lines, respectively. From the mappings and the spectra in Figures 15-16, these three *IRDCs* may have the infall motions in the large-scaled regions. We estimate the extent of the infall signature to be up to $2 \times 2\ \text{arcmin}^2$ (at least 2.11 pc for *IRDC* G331.035-00.418, 1.10 pc for *IRDC* G331.708+00.583 and 1.40 pc for *IRDC* G341.942-00.167). In addition, for *IRDC* G331.708+00.583, Cyganowski et al. (2008) detected it as an outflow candidate and Yu & Wang (2012) found that it has two outflows, corresponding to the two cores in the cloud. At the same time, for *IRDC* G331.035-00.418 and *IRDC* G341.942-00.167, we plot their P-V diagrams and do not find the outflow signatures. Infall and outflow both are the sign of star forming. Hence, we suggest that *IRDC* G331.035-00.418, *IRDC* G341.942-00.167 and *IRDC* G331.708+00.583 are forming stars, while other *IRDCs* without the star-forming activity may be in much earlier stage.

4.2 The integrated intensity

Ratios of the average integrated intensity of N_2H^+ , HNC and HCO^+ to HCN for each *IRDC* are presented in Table 3. Considering the accuracy of the ratios, we chose the pixels with the inte-

grated intensity $> 5\sigma$ and the intensity $> 3\sigma$ for N_2H^+ , HNC, HCO^+ , and HCN. From Table 3, we find that all $I_{\text{HCO}^+/\text{HCN}}$, $I_{\text{N}_2\text{H}^+/\text{HCN}}$, and $I_{\text{HNC}/\text{HCN}}$ are almost a constant with around 1.5 in the error scales for all the *IRDCs*, implying that the integrated intensity ratios seem not to change with the evolution of *IRDCs*. Hsieh et al. (2012) shows that $I_{\text{HNC}/\text{HCO}^+}$ is 1.67 ± 0.83 in the starburst Ring and 2.22 ± 0.50 in the Syfert nucleus. It is noticeable to us that our $I_{\text{HNC}/\text{HCO}^+}$ of each *IRDC* is very different from those of the starburst Ring and the Syfert nucleus, indicating that the integrated intensity ratios probably depend on the cloud environments.

Figure 17 shows a relationship of the average integrated intensity between HNC, HCO^+ lines and HCN line for the 14 *IRDCs*. We find a tight correlation between HCO^+ and HCN ($r = 0.98$), and a linear fitting relationship:

$$I_{\text{HCO}^+} = (1.32 \pm 0.04) \times I_{\text{HCN}} + (0.49 \pm 0.10) \quad (2)$$

A very high correlation coefficient $r = 0.90$ is also found for the average integrated intensity of HNC and HCN lines (Figure 17) for the 14 *IRDCs*. The linear fitting result is

$$I_{\text{HNC}} = (0.77 \pm 0.03) \times I_{\text{HCN}} + (1.75 \pm 0.10) \quad (3)$$

The results above indicate that there is a close relationship for the three species during the process of their chemical evolution in the *IRDCs*. According to this argument, it will contribute to determine the dominated chemistry model in the *IRDCs* through the numerical simulation. From Figure 17, we also find that *IRDCs* G331.035-00.418 and G341.942-00.167 have larger integrated intensity of HNC, HCO^+ , and HCN, which are associated with an UCHII region. It seems that the *UV* radiation field has an influence on the chemistry of HNC, HCO^+ , and HCN molecules in the *IRDCs*, but we need more data to examine this result.

4.3 Column density and the relationships between the abundance ratios and distances

4.3.1 Derivation of physical parameters

Under an assumption of local thermodynamic equilibrium (LTE), the total column density, N , of the molecule can be derived from the following formula (Scoville et al. 1986).

$$N = 10^5 \times \frac{3k^2}{4h\pi^3\mu^2\nu^2} \exp\left(\frac{h\nu J}{2kT_{\text{ex}}}\right) \frac{T_{\text{ex}} + h\nu/6k(J+1)}{\exp(-h\nu/kT_{\text{ex}})} \times \int \frac{\tau_\nu}{1 - e^{-\tau_\nu}} T_{\text{mb}} dv \quad (4)$$

where k is the Boltzmann constant, h is the Planck constant, μ is the permanent dipole moment of the molecule and J is the rotational quantum number of the lower state. Here the permanent dipole moment μ of N_2H^+ , HNC, HCO^+ and HCN molecules are 3.40, 3.05, 3.90, and 2.985^2 (Müller et al. 2001, 2005), respectively. ν is the transition frequency, T_{ex} is the excitation temperature, T_{mb} is the main beam brightness temperature which we get from the Gauss fits, and τ_ν is the optical depth.

Since N_2H^+ and HCN lines show their hyperfine structures, we can obtain their τ_ν from the HFS fits. The fitted results are listed in Table 1 column 8. The main brightness temperature T_{mb} is given by:

$$T_{\text{mb}} = f[J(T_{\text{ex}}) - J(T_{\text{bg}})](1 - e^{-\tau_\nu}) \quad (5)$$

where f is the filling factor, here we assume $f = 1$ for all the molecules, T_{bg} is the background temperature, and $J(T)$ is defined by

$$J(T) = \frac{h\nu}{k} \frac{1}{\exp(h\nu/kT) - 1} \quad (6)$$

According to equation (5) and equation (6), we can derive T_{ex} and τ_ν as below:

$$T_{\text{ex}} = \frac{h\nu}{k} \left(\ln\left(1 + \frac{h\nu}{k} \left[\frac{T_{\text{mb}}}{f(1 - \exp(-\tau_\nu))} + J(T_{\text{bg}}) \right]^{-1} \right) \right)^{-1} \quad (7)$$

$$\tau_\nu = -\ln\left\{1 - \frac{T_{\text{mb}}}{f} [J(T_{\text{ex}}) - J(T_{\text{bg}})]^{-1}\right\} \quad (8)$$

So T_{ex} for N_2H^+ and HCN can be obtained from equation (7). But for HNC and HCO^+ , we assume that they have the same excitation temperature to HCN, because they show a tight correlation in their integrated intensity. Then the optical depth τ_ν of HNC and HCO^+ can be derived from equation (8). T_{ex} and τ_ν of the four molecules are showed in Table 1 and Table 2. Then we can calculate the column densities of N_2H^+ , HNC, HCO^+ and HCN using equation (4), the results are in Table 4.

4.3.2 The Column density of N_2H^+ , HNC, HCO^+ , HCN and abundance ratios

Using the equations in section 4.3.1, all the physical parameters are derived and presented in Tables 1-4. From Table 1 and Table 2, we find that $T_{\text{ex}} < 25$ K and the optical depths of the four molecular lines are less than 1 for all the *IRDCs*. Considering the fact that HNC, HCO^+ and HNC lines should be optically thick, their optical depths in our results are probably underestimated. The derived column densities for the four species and the abundance ratios $N_{\text{HNC}}/N_{\text{HCN}}$, $N_{\text{HCO}^+}/N_{\text{HCN}}$, $N_{\text{HNC}}/N_{\text{HCO}^+}$ are listed in Table 4. The uncertainties of the column densities include all the errors caused by T_{ex} , opacities and the integrated intensities. From Table 4, we find that the column densities of the four molecules spread over the range of $10^{12} \sim 10^{13}$. Then we estimate that the abundances of the four molecules using the typical H_2 column density $(0.9 \sim 4.6) \times 10^{22} \text{ cm}^{-2}$ in southern infrared dark clouds (Vasyunina et al. 2009) are in the range of $10^{-11} \sim 10^{-9}$, which are consistent with the results of Vasyunina et al. (2011) and Zinchenko et al. (2009) for N_2H^+ , HNC and HCN molecules, but \sim one order lower for HCO^+ molecule, even over two order lower than the results of Sanhueza et al. (2012). This abundant difference of HCO^+ molecule is mainly caused by the optical depth. HCO^+ line is optically thin in our study. From the abundance ratios of HNC, HCO^+ , and HCN for each *IRDC* in Table 4, we find that HNC is more abundant than HCO^+ and HCN, except for *IRDC* G331.035-00.418, which agree with the fact that HNC molecule is the tracer of the cold gas. And the derived $N_{\text{HNC}}/N_{\text{HCN}} = 1.47 \pm 0.50$ is consistent with the results in the dark cloud cores (Hirota et al. 1998). $N_{\text{HCN}}/N_{\text{HCO}^+}$ is approximately equal to 1, implying the similar origin and chemistry evolution of these two molecules. Furthermore, we also calculate the average abundance ratios ($N_{\text{HNC}}/N_{\text{HCN}}$, $N_{\text{HNC}}/N_{\text{HCO}^+}$ and $N_{\text{HCN}}/N_{\text{HCO}^+}$) of the 14 southern *IRDCs*, which are presented in Table 5. From Table 5, we find that $N_{\text{HCN}}/N_{\text{HCO}^+}$ is almost the same in the error scale in the three different environments, suggesting that the abundance ratio of HCN to HCO^+ may be not affected by the environments. The differences of other two ratios $N_{\text{HNC}}/N_{\text{HCN}}$ and $N_{\text{HNC}}/N_{\text{HCO}^+}$ indicate that *IRDCs* may represent the chemistry of earlier star formation.

² <http://www.astro.uni-koeln.de/cdms/entries>

Table 4. The column density of N_2H^+ , HNC, HCO^+ and HCN and the abundance ratios of HNC, HCO^+ and HCN.

Source	$\text{N}_{\text{N}_2\text{H}^+}$ ($\times 10^{12}$) cm^{-2}	N_{HNC} ($\times 10^{12}$) cm^{-2}	N_{HCO^+} ($\times 10^{12}$) cm^{-2}	N_{HCN} ($\times 10^{12}$) cm^{-2}	$\text{N}_{\text{HNC}}/\text{N}_{\text{HCN}}$	$\text{N}_{\text{HCO}^+}/\text{N}_{\text{HCN}}$	$\text{N}_{\text{HNC}}/\text{N}_{\text{HCO}^+}$
G003.399-00.399	11.40 \pm 1.15	9.27 \pm 0.87	4.38 \pm 0.51	6.29 \pm 4.03	1.47 \pm 0.95	0.70 \pm 0.45	2.12 \pm 0.32
G003.436-00.572	4.90 \pm 0.64	5.76 \pm 0.54	2.29 \pm 0.30	4.16 \pm 1.32	1.38 \pm 0.46	0.55 \pm 0.19	2.52 \pm 0.41
G010.402-00.202	7.75 \pm 0.65	6.66 \pm 0.55	4.73 \pm 0.38	5.08 \pm 1.63	1.31 \pm 0.43	0.93 \pm 0.31	1.41 \pm 0.16
G010.990-00.083	6.55 \pm 0.62	5.99 \pm 0.45	2.44 \pm 0.26	2.93 \pm 1.07	2.04 \pm 0.76	0.83 \pm 0.32	2.45 \pm 0.32
G308.121-00.152	4.35 \pm 0.53	8.01 \pm 0.58	5.96 \pm 0.41	5.47 \pm 1.40	1.46 \pm 0.39	1.09 \pm 0.29	1.34 \pm 0.13
G317.701+00.110	7.03 \pm 0.76	6.34 \pm 0.58	3.91 \pm 0.36	3.05 \pm 1.12	2.08 \pm 0.79	1.28 \pm 0.49	1.62 \pm 0.21
G321.756+00.029	6.83 \pm 0.75	6.64 \pm 0.61	5.24 \pm 0.44	6.04 \pm 1.38	1.10 \pm 0.27	0.87 \pm 0.21	1.27 \pm 0.16
G331.035-00.418	12.90 \pm 0.92	11.40 \pm 1.03	13.10 \pm 1.68	16.10 \pm 2.12	0.71 \pm 0.11	0.81 \pm 0.15	0.87 \pm 0.14
G331.708+00.583	26.50 \pm 1.44	6.87 \pm 0.71	4.43 \pm 0.48	6.60 \pm 2.20	1.04 \pm 0.36	0.67 \pm 0.24	1.55 \pm 0.23
G334.198-00.202	5.08 \pm 0.54	5.32 \pm 0.46	2.24 \pm 0.27	2.92 \pm 1.15	1.82 \pm 0.73	0.77 \pm 0.32	2.38 \pm 0.35
G337.764-00.338	11.10 \pm 0.75	10.60 \pm 0.71	4.29 \pm 0.36	4.69 \pm 0.86	2.26 \pm 0.44	0.91 \pm 0.18	2.47 \pm 0.27
G341.942-00.167	20.20 \pm 1.36	16.00 \pm 1.25	12.20 \pm 0.96	15.30 \pm 2.93	1.05 \pm 0.22	0.80 \pm 0.17	1.31 \pm 0.15
G344.726-00.541	3.26 \pm 0.59	4.35 \pm 0.41	2.82 \pm 0.28	2.53 \pm 0.94	1.72 \pm 0.66	1.11 \pm 0.43	1.54 \pm 0.21
G345.556+00.026	3.35 \pm 0.69	4.07 \pm 0.42	2.76 \pm 0.28	3.58 \pm 1.03	1.14 \pm 0.35	0.77 \pm 0.24	1.47 \pm 0.21

Table 5. The average abundance ratios among different environments

Environment	$\text{N}_{\text{HNC}}/\text{N}_{\text{HCN}}$	$\text{N}_{\text{HNC}}/\text{N}_{\text{HCO}^+}$	$\text{N}_{\text{HCN}}/\text{N}_{\text{HCO}^+}$	References
IRDCS	1.47 \pm 0.50	1.74 \pm 0.23	1.21 \pm 0.41	Present work
ISM	0.21 \pm 0.05	—	1.47 \pm 0.86	Liszt & Lucas (2001)
Star forming regions	0.21 \pm 0.06	0.5 \pm 0.3	1.9 \pm 0.9	Godard et al. (2010)

4.3.3 The relationship between abundance ratios and distances

Figure 18 shows the relationships between the average abundance ratios and the distances of the 14 southern *IRDCs*. $\text{N}_{\text{HCO}^+}/\text{N}_{\text{HCN}}$, $\text{N}_{\text{HCO}^+}/\text{N}_{\text{HNC}}$ and $\text{N}_{\text{HCN}}/\text{N}_{\text{HNC}}$ all show a linear relationship with the distances. The relationships are:

$$\text{N}_{\text{HCO}^+}/\text{N}_{\text{HCN}} = (0.06 \pm 0.07) \times d + (0.66 \pm 0.21) \quad (9)$$

$$\text{N}_{\text{HCO}^+}/\text{N}_{\text{HNC}} = (0.03 \pm 0.03) \times d + (0.47 \pm 0.07) \quad (10)$$

$$\text{N}_{\text{HCN}}/\text{N}_{\text{HNC}} = (0.03 \pm 0.08) \times d + (0.56 \pm 0.23) \quad (11)$$

From above relationships, we find the abundance ratios O/N increasing slowly with the distances of the *IRDCs*, and a small increase is also found for the abundance ratio $\text{N}_{\text{HCN}}/\text{N}_{\text{HNC}}$ to the distance. Since the errors and limit data, the more studies should be done to check this conclusion.

5 SUMMARY

We do the research of 14 southern *IRDCs* with $\text{N}_2\text{H}^+(1-0)$, HNC(1-0), $\text{HCO}^+(1-0)$, and HCN(1-0) lines of the *MALT90* survey and *Spitzer* 8 μm , 24 μm data. The integrated intensity diagrams of the four molecular lines are mapped and the physical parameters are obtained for the 14 southern *IRDCs*. We also discuss the kinetic processes and explore the chemical features. Our main results are summarized as follows.

1. The *Spitzer* images show that the 14 *IRDCs* are in different evolutionary stages, from "starless cores" with no IR emissions to "red cores" with the strong 8 μm emission.

2. According to the optically thick HNC and HCO^+ line profiles and mappings, three *IRDCs* (*IRDC* G331.035-00.418, G331.708+00.583, and G341.942-00.167) are found to have the in-fall motions, while other *IRDCs* without the star-forming activity may be in much earlier stage.

3. The integrated intensity of HNC, HCO^+ and HCN correlate well with each other for the 14 *IRDCs*, implying a close link to their chemistry evolution in the *IRDCs*.

4. The obtained physical parameters show that $T_{\text{ex}} < 25$ K

for all the 14 *IRDCs* and N_2H^+ line is optically thin in the *IRDCs*. The column densities of the four molecules span up to two orders $10^{12} \sim 10^{13}$ and their corresponding abundances are in the range of 10^{-11} to 10^{-9} . The average abundance ratios $\text{N}_{\text{HNC}}/\text{N}_{\text{HCN}} = 1.47 \pm 0.50$, $\text{N}_{\text{HNC}}/\text{N}_{\text{HCO}^+} = 1.74 \pm 0.22$ show significant difference with those of ISM and star forming regions, indicating that the environment of earlier star formation may be different. However, $\text{N}_{\text{HCN}}/\text{N}_{\text{HCO}^+} = 1.24 \pm 0.41$ is almost the same with that of the other environments, suggesting that the abundance ratio of HCN to HCO^+ may be not affected by the environment.

ACKNOWLEDGMENTS

We thank the anonymous referee for whose constructive suggestions. This research has made use of the data products from the *Millimetre Astronomy Legacy Team 90 GHz (MALT90)* survey, and also used NASA/IPAC Infrared Science Archive, which is operated by the Jet Propulsion Laboratory, California Institute of Technology, under contract with the National Aeronautics and Space Administration.

REFERENCES

- Bergin, E. A., Ciardi, D. R., Lada, C. J., Alves, J., & Lada, E. A. 2001, *ApJ*, 557, 209
- Beuther, H., Sridharan, T. K., & Saito, M. 2005, *ApJ*, 634, L185
- Bronfman, L., Nyman, L.-A., & May, J. 1996, *A&AS*, 115, 81
- Carey, S. J., Clark, F. O., Egan, M. P., et al. 1998, *ApJ*, 508, 721
- Carey, S. J., Feldman, P. A., Redman, R. O., et al. 2000, *ApJ*, 543, L157
- Chambers, E. T., Jackson, J. M., Rathborne, J. M., & Simon, R. 2009, *ApJS*, 181, 360
- Cyganowski, C. J., Whitney, B. A., Holden, E., et al. 2008, *AJ*, 136, 2391
- Egan, M. P., Shipman, R. F., Price, S. D., et al. 1998, *ApJ*, 494, L199
- Fazio, G. G., Hora, J. L., Allen, L. E., et al. 2004, *ApJS*, 154, 10

- Foster, J. B., Jackson, J. M., Barnes, P. J., et al. 2011, *ApJS*, 197, 25
- Fuller, G. A., Williams, S. J., & Sridharan, T. K. 2005, *Protostars and Planets V*, 8559
- Godard, B., Falgarone, E., Gerin, M., Hily-Blant, P., & de Luca, M. 2010, *A&A*, 520, A20
- Hirota, T., Yamamoto, S., Mikami, H., & Ohishi, M. 1998, *ApJ*, 503, 717
- Hsieh, P.-Y., Ho, P. T. P., Kohno, K., Hwang, C.-Y., & Matsushita, S. 2012, *ApJ*, 747, 90
- Jackson, J. M., Finn, S., Rathborne, J., Chambers, E., & Simon, R. 2008, *Bulletin of the American Astronomical Society*, 40, 267
- Jones, P. A., Burton, M. G., Cunningham, M. R., et al. 2012, *MNRAS*, 419, 2961
- Ladd, N., Purcell, C., Wong, T., & Robertson, S. 2005, *PASA*, 22, 62
- Lis, D. C., & Carlstrom, J. E. 1994, *ApJ*, 424, 189
- Liszt, H., & Lucas, R. 2001, *A&A*, 370, 576
- Lo, N., Cunningham, M. R., Jones, P. A., et al. 2009, *MNRAS*, 395, 1021
- Mardones, D., Myers, P. C., Tafalla, M., et al. 1997, *apj*, 489, 719
- Müller, H. S. P., Thorwirth, S., Roth, D. A., & Winnewisser, G. 2001, *A&A*, 370, L49
- Müller, H. S. P., Schlöder, F., Stutzki, J., & Winnewisser, G. 2005, *Journal of Molecular Structure*, 742, 215
- Peretto, N., & Fuller, G. A. 2009, *VizieR Online Data Catalog*, 350, 50405
- Perrault, M., Omont, A., Simon, G., et al. 1996, *A&A*, 315, L165
- Rathborne, J. M., Chambers, E. T., Jackson, J. M., & Simon, R. 2005, *Bulletin of the American Astronomical Society*, 37, #184.18
- Rathborne, J. M., Jackson, J. M., & Simon, R. 2006, *ApJ*, 641, 389
- Rawlings, J. M. C., Redman, M. P., Keto, E., & Williams, D. A. 2004, *MNRAS*, 351, 1054
- Redman, R. O., Feldman, P. A., Wyrowski, F., et al. 2003, *ApJ*, 586, 1127
- Reid, M. J., Menten, K. M., Zheng, X. W., et al. 2009, *ApJ*, 700, 137
- Requena-Torres, M. A., Martín-Pintado, J., Rodríguez-Franco, A., et al. 2006, *A&A*, 455, 971
- Sanhueza, P., Jackson, J.M., Foster, J.B., Garay, G., Silva, A., Finn, S.C. 2012, *arXiv:1206.6500v1*
- Scoville, N.Z., Sargent, A.I., Sanders, D.B. et al. 1986, *ApJ*, 303, 416
- Simon, R., Jackson, J. M., Rathborne, J. M., & Chambers, E. T. 2006, *ApJ*, 639, 227
- Vasyunina, T., Linz, H., Henning, T., et al. 2009, *A&A*, 499, 149
- Vasyunina, T., Linz, H., Henning, T., et al. 2011, *A&A*, 527, A88
- Werner, M. W., Roellig, T. L., Low, F. J., et al. 2004, *ApJS*, 154, 1
- Yu, N.P. & Wang, J.J. *RAA* in press
- Zinchenko, I., Caselli, P., & Pirogov, L. 2009, *MNRAS*, 395, 2234

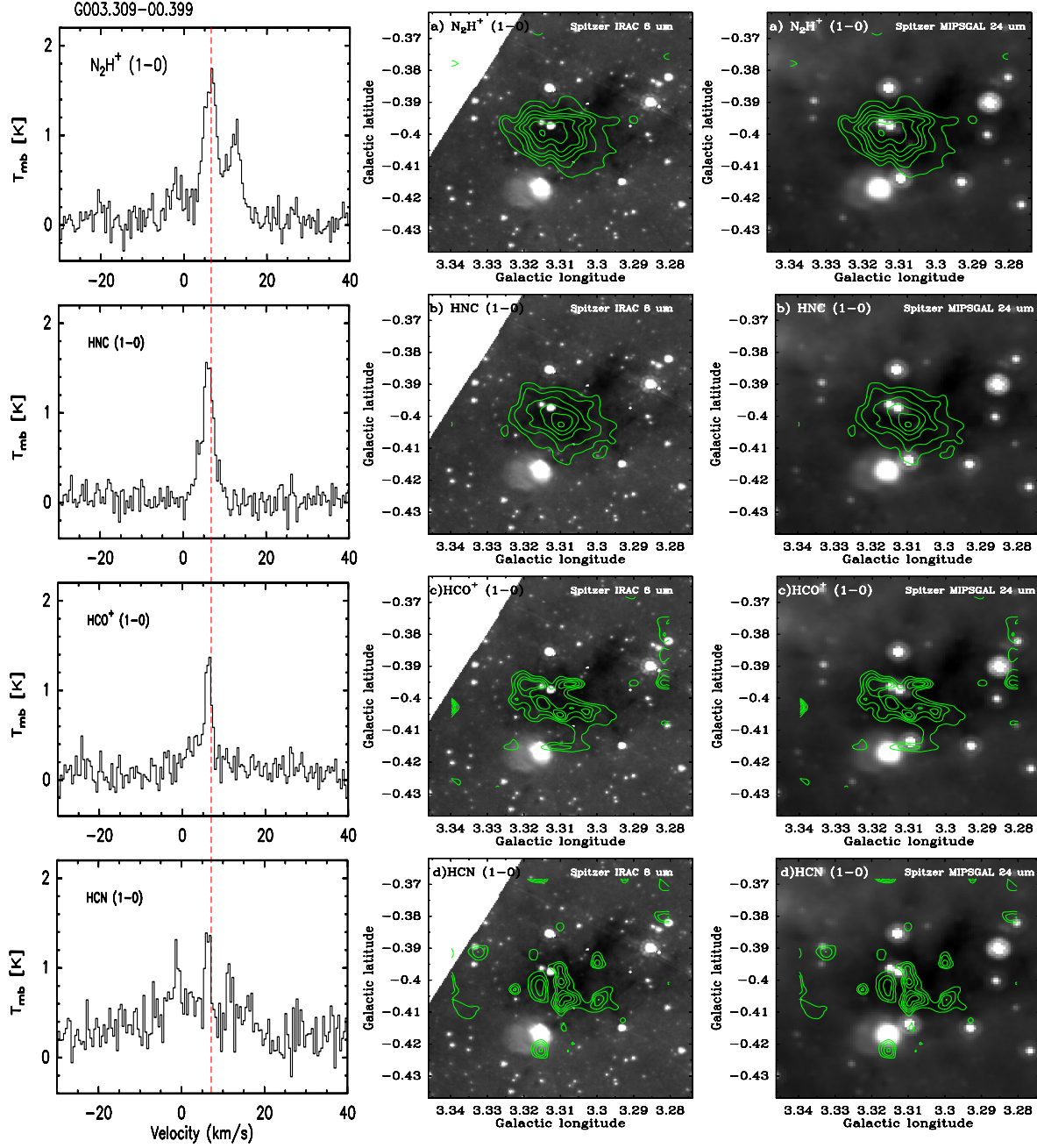


Figure 1. The spectra and the integrated intensity maps of N_2H^+ , HNC, HCO^+ , and HCN in IRDC G003.309-00.399. The spectra are in the left; the grayscale in the middle plane is *Spitzer* IRAC 8 μm and that in the right plane is *Spitzer* MIPS GAL 24 μm . The red dash line represents the V_{LSR} of N_2H^+ line

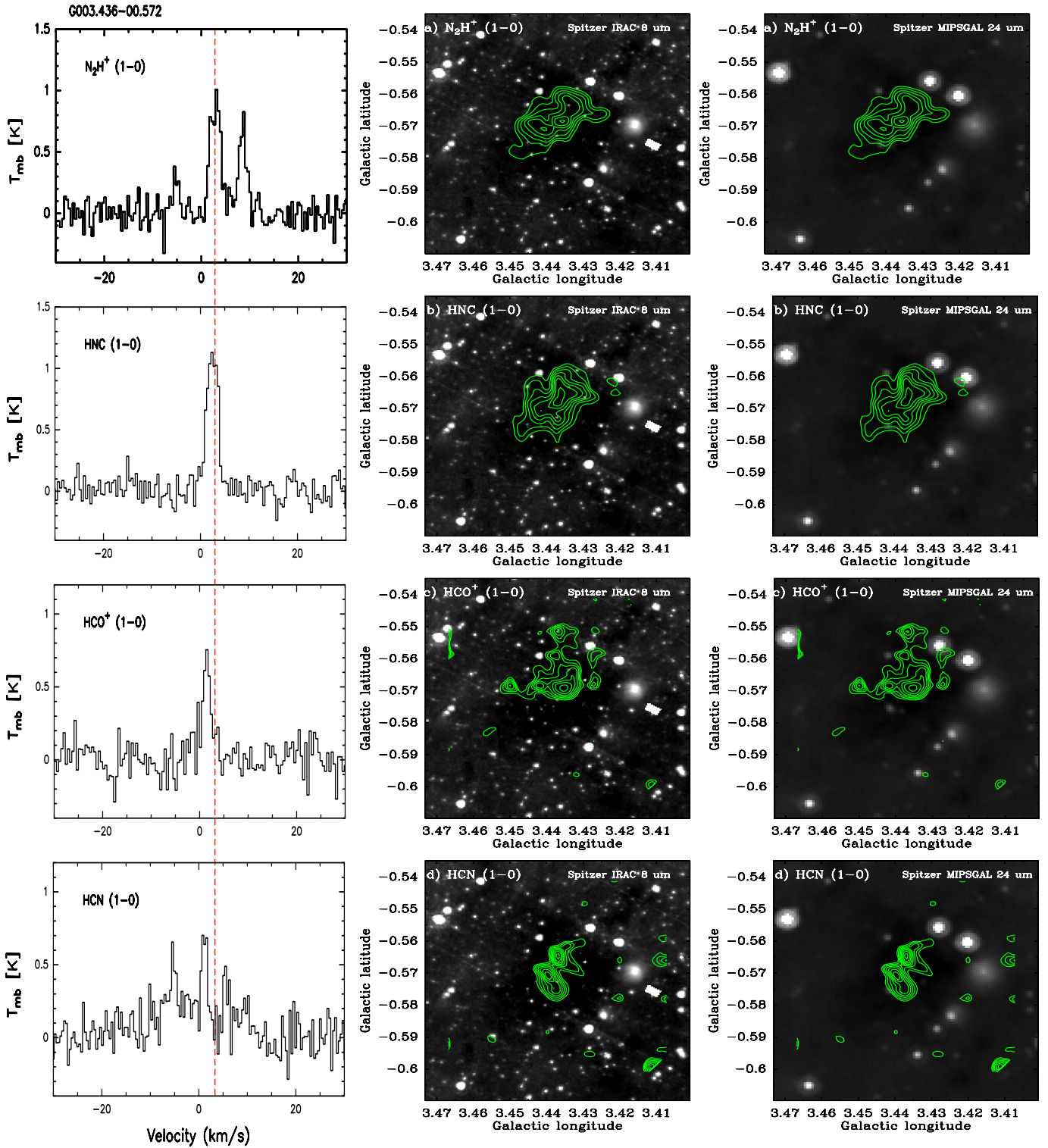


Figure 2. The spectra and the integrated intensity maps of N_2H^+ , HNC, HCO^+ , and HCN in IRDC G003.436-00.572. The spectra are in the left; the grayscale in the middle plane is *Spitzer* IRAC 8 μm and that in the right plane is *Spitzer* MIPS GAL 24 μm . The red dash line represents the V_{LSR} of N_2H^+ line

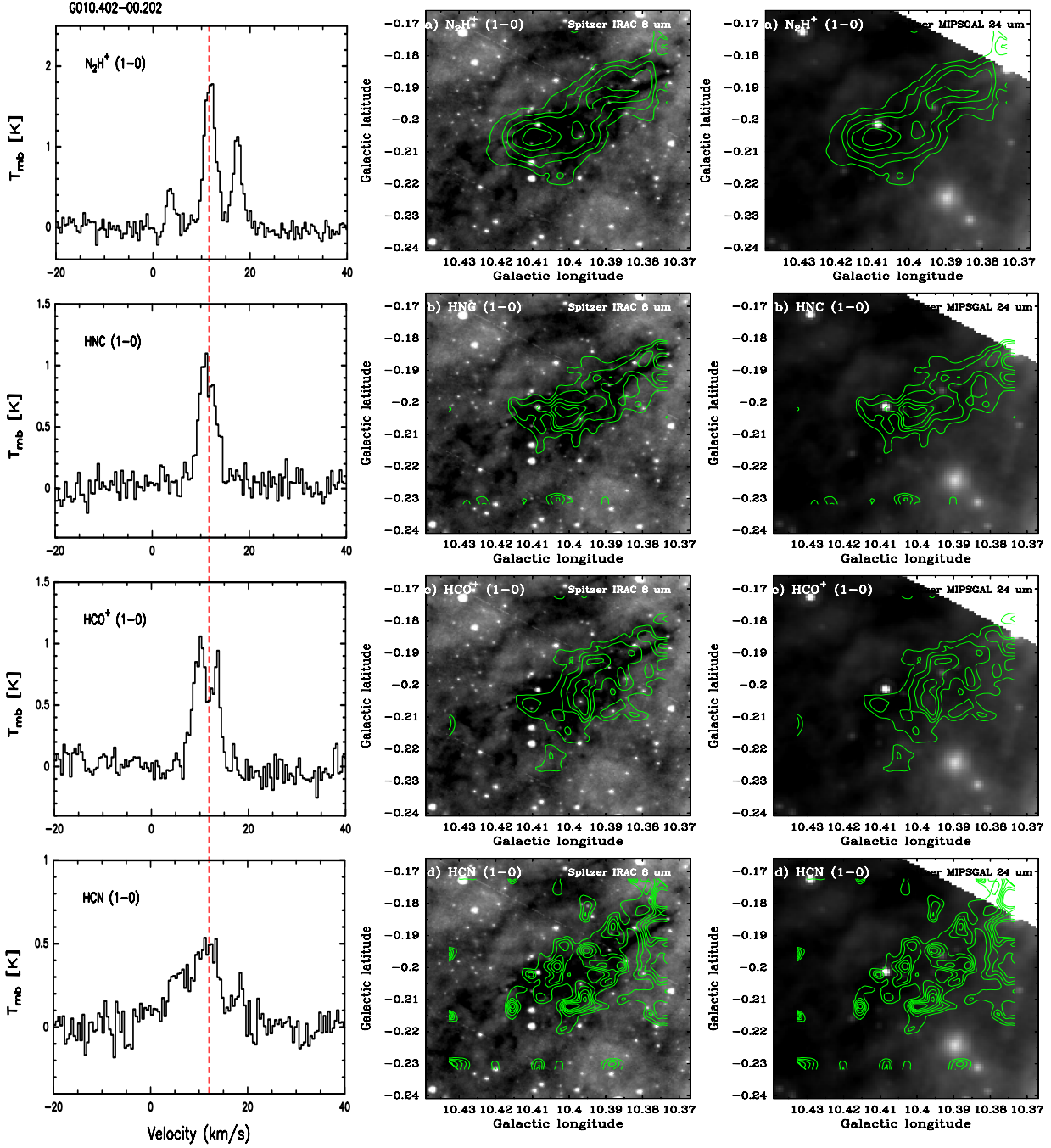


Figure 3. The spectra and the integrated intensity maps of N_2H^+ , HNC, HCO^+ , and HCN in IRDC G010.402-00.202. The spectra are in the left; the grayscale in the middle plane is *Spitzer* IRAC 8 μm and that in the right plane is *Spitzer* MIPS GAL 24 μm . The red dash line represents the V_{LSR} of N_2H^+ line

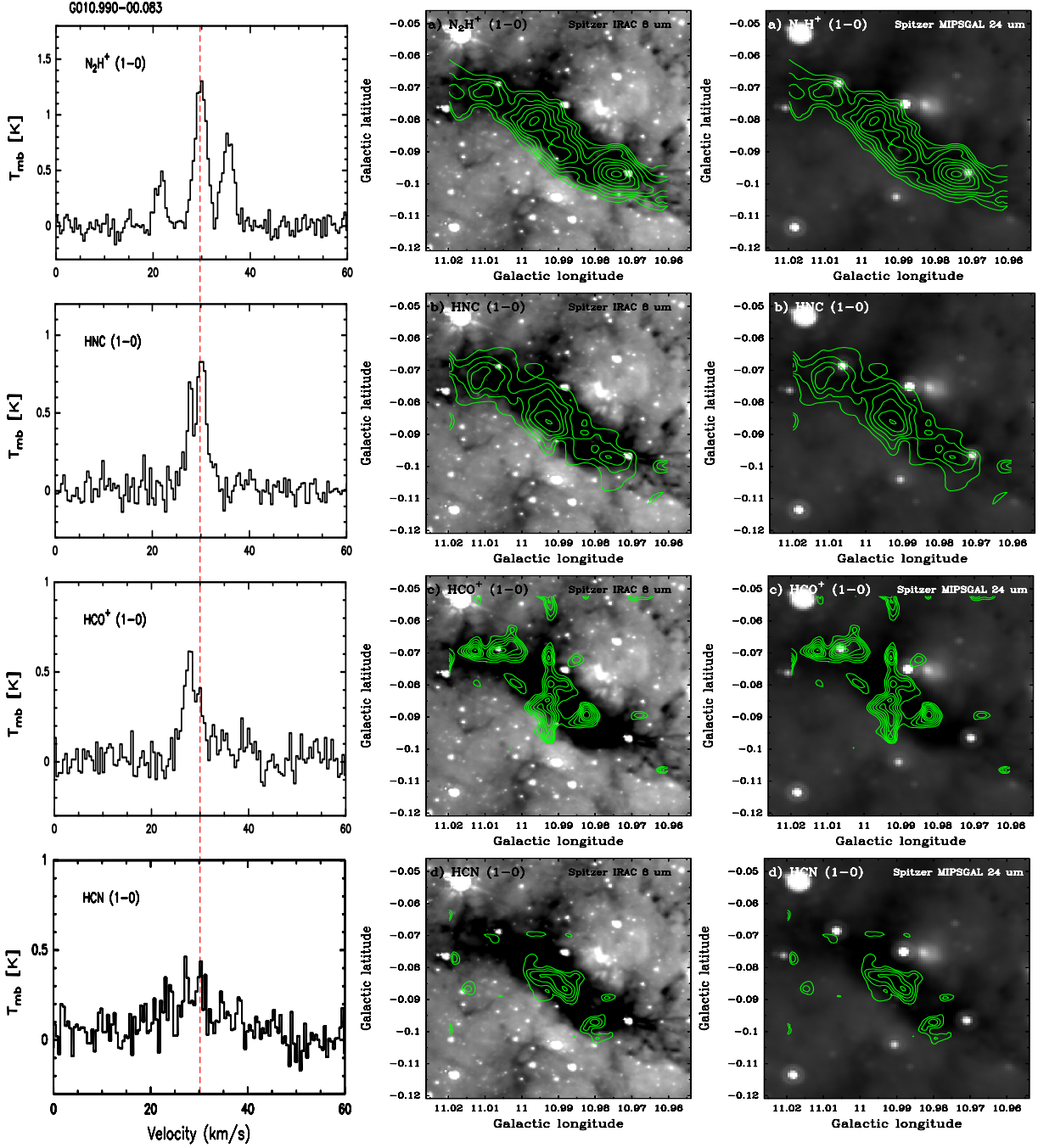


Figure 4. The spectra and the integrated intensity maps of N_2H^+ , HNC, HCO^+ , and HCN in IRDC G010.990-00.083. The spectra are in the left; the grayscale in the middle plane is *Spitzer IRAC* $8 \mu\text{m}$ and that in the right plane is *Spitzer MIPS GAL* $24 \mu\text{m}$. The red dash line represents the V_{LSR} of N_2H^+ line

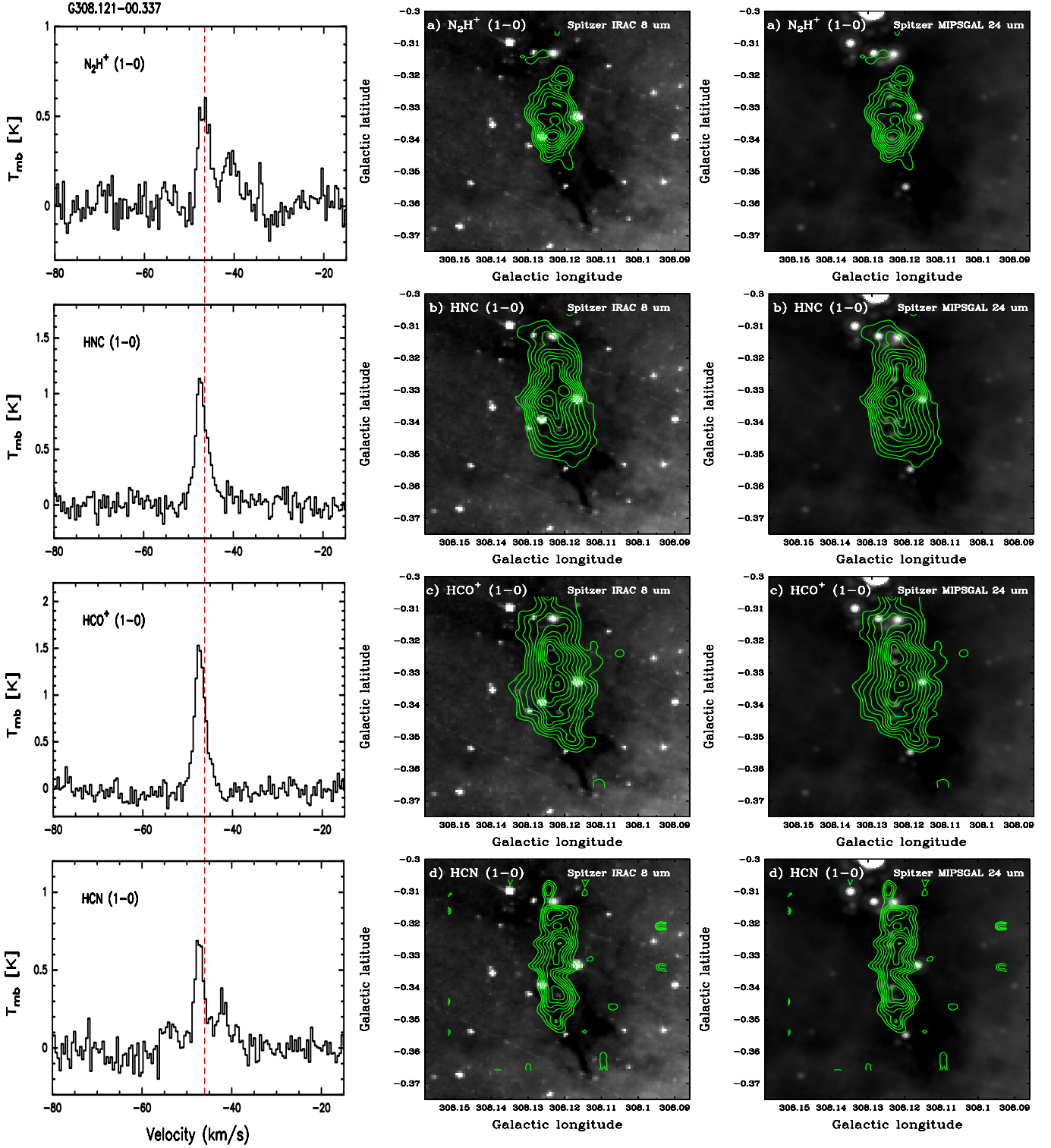


Figure 5. The spectra and the integrated intensity maps of N_2H^+ , HNC, HCO^+ , and HCN in IRDC G308.121-00.152. The spectra are in the left; the grayscale in the middle plane is *Spitzer* IRAC 8 μm and that in the right plane is *Spitzer* MIPS GAL 24 μm . The red dash line represents the V_{LSR} of N_2H^+ line

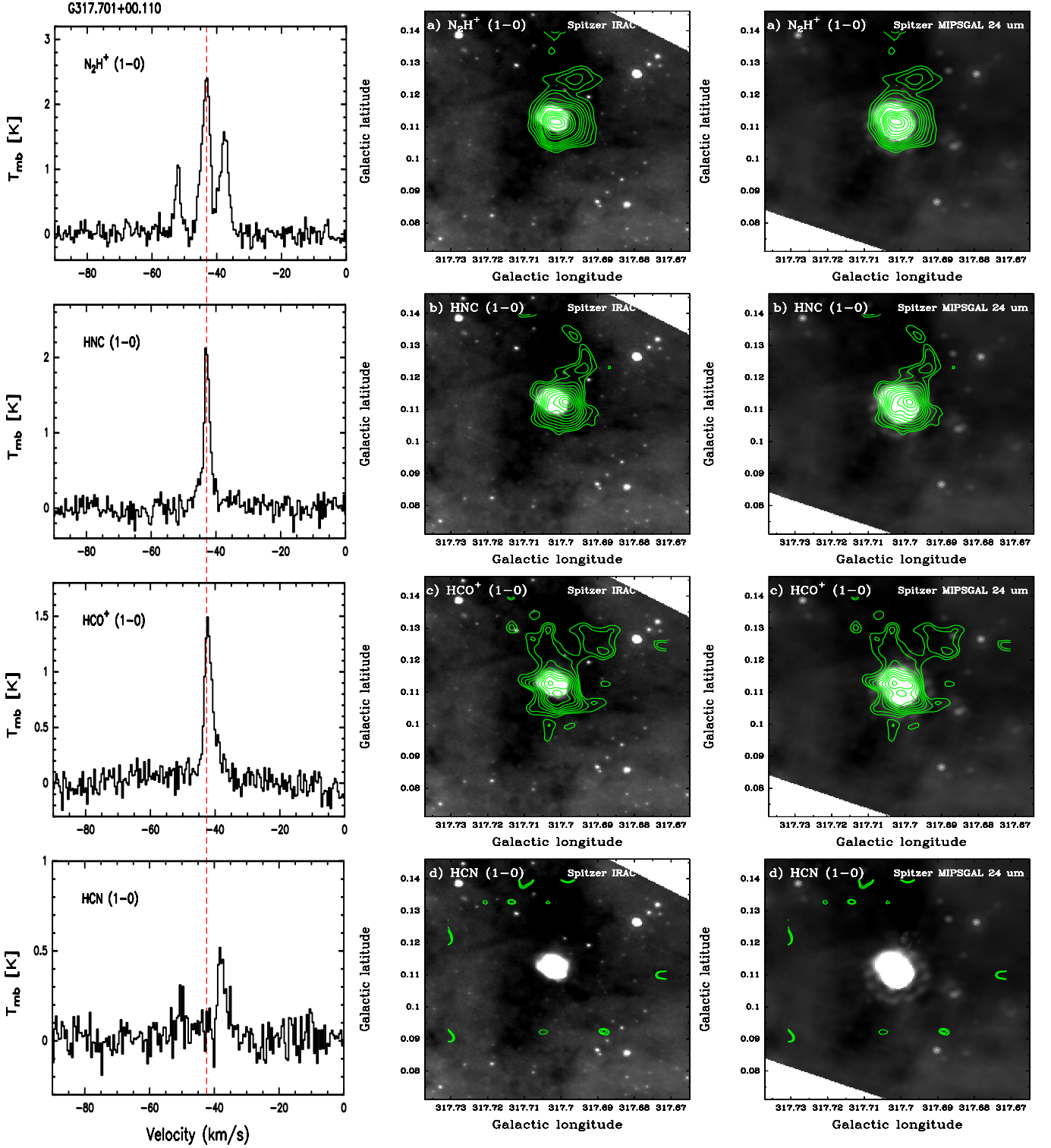


Figure 6. The spectra and the integrated intensity maps of N_2H^+ , HNC, HCO^+ , and HCN in IRDC G317.701+00.110. The spectra are in the left; the grayscale in the middle plane is *Spitzer* IRAC 8 μm and that in the right plane is *Spitzer* MIPS GAL 24 μm . The red dash line represents the V_{LSR} of N_2H^+ line

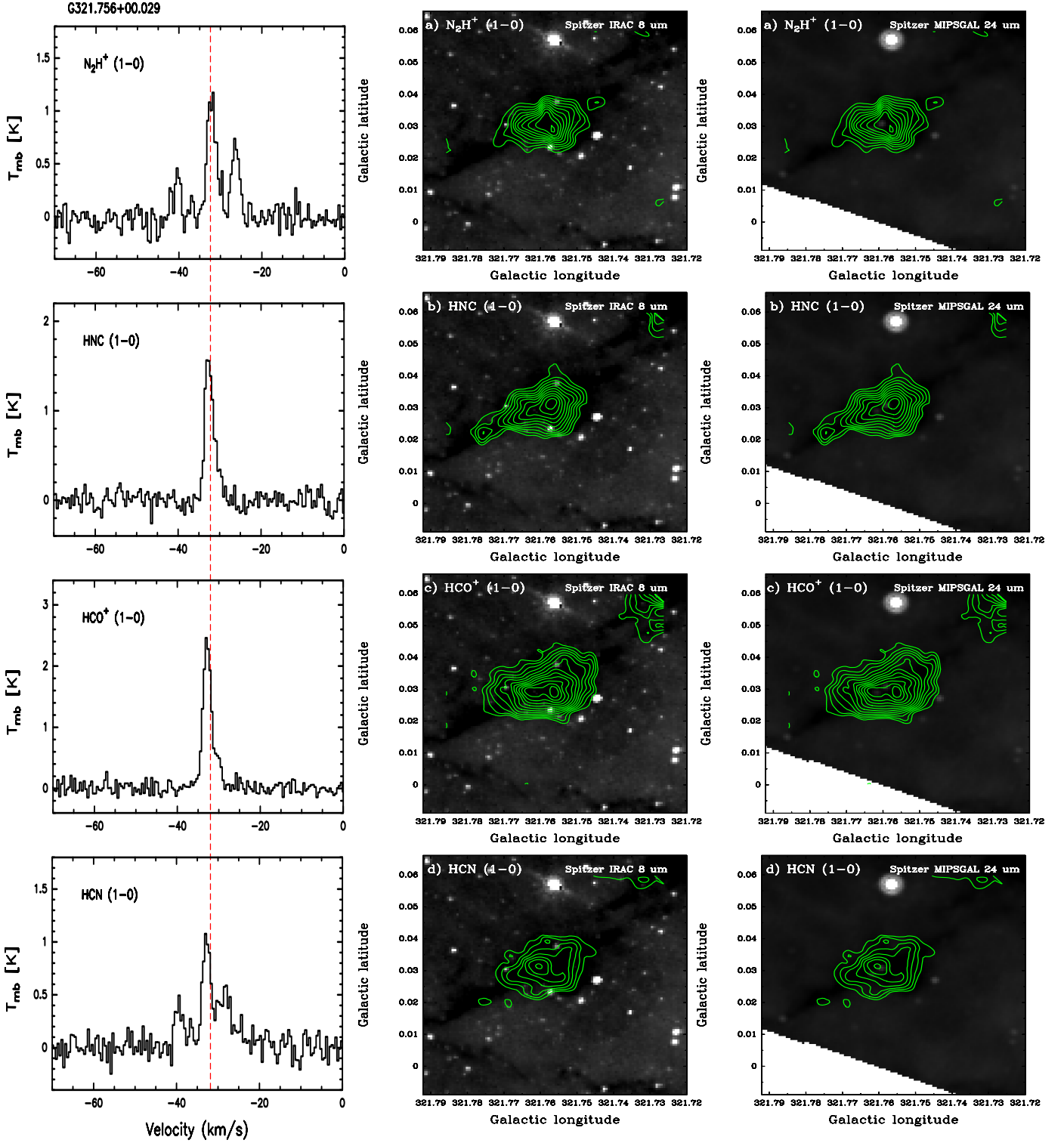


Figure 7. The spectra and the integrated intensity maps of N_2H^+ , HNC, HCO^+ , and HCN in IRDC G321.756+00.029. The spectra are in the left; the grayscale in the middle plane is *Spitzer* IRAC 8 μm and that in the right plane is *Spitzer* MIPS GAL 24 μm . The red dash line represents the V_{LSR} of N_2H^+ line

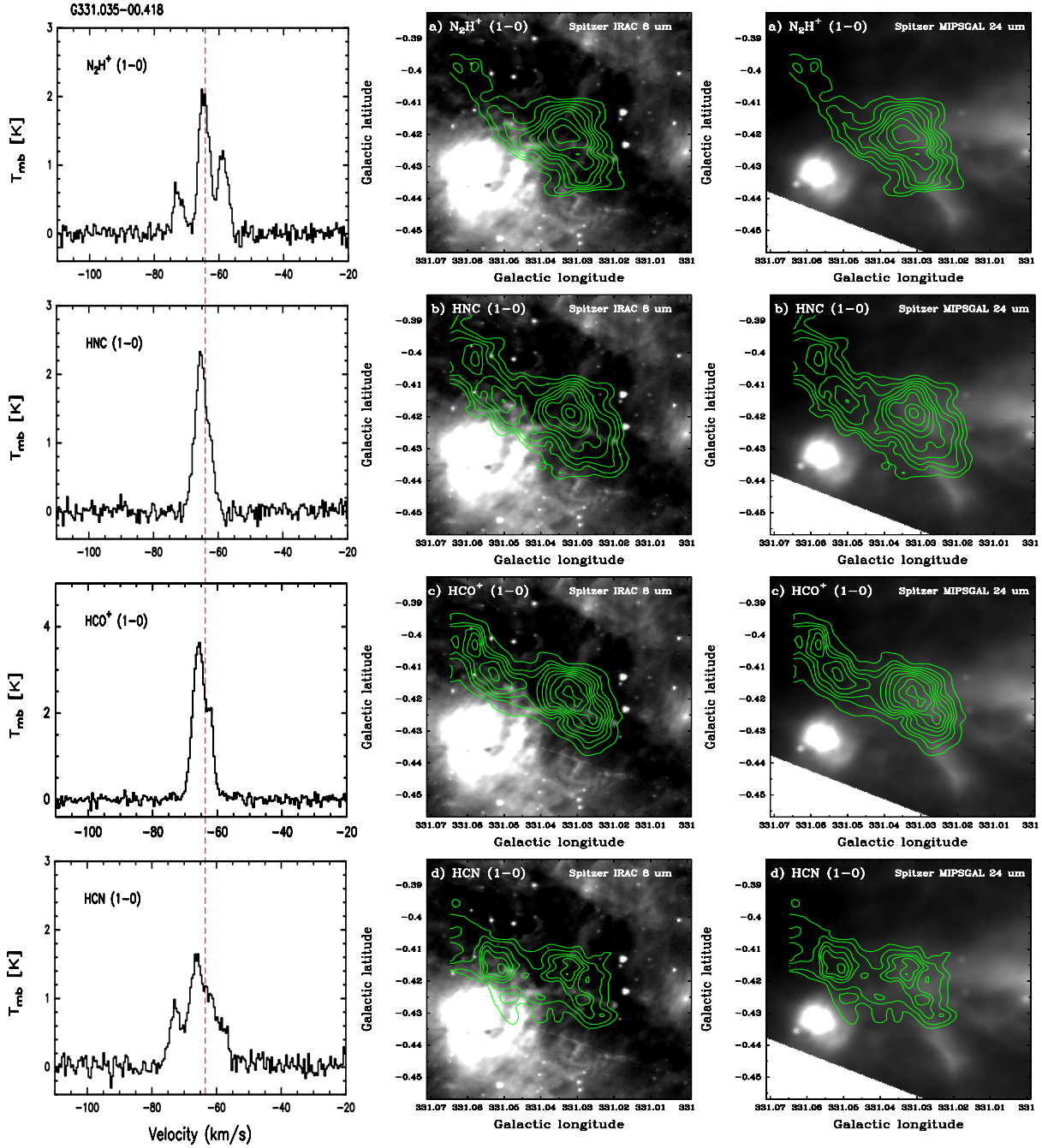


Figure 8. The spectra and the integrated intensity maps of N_2H^+ , HNC, HCO^+ , and HCN in IRDC G331.035-00.418. The spectra are in the left; the grayscale in the middle plane is *Spitzer* IRAC 8 μm and that in the right plane is *Spitzer* MIPSGAL 24 μm . The red dash line represents the V_{LSR} of N_2H^+ line

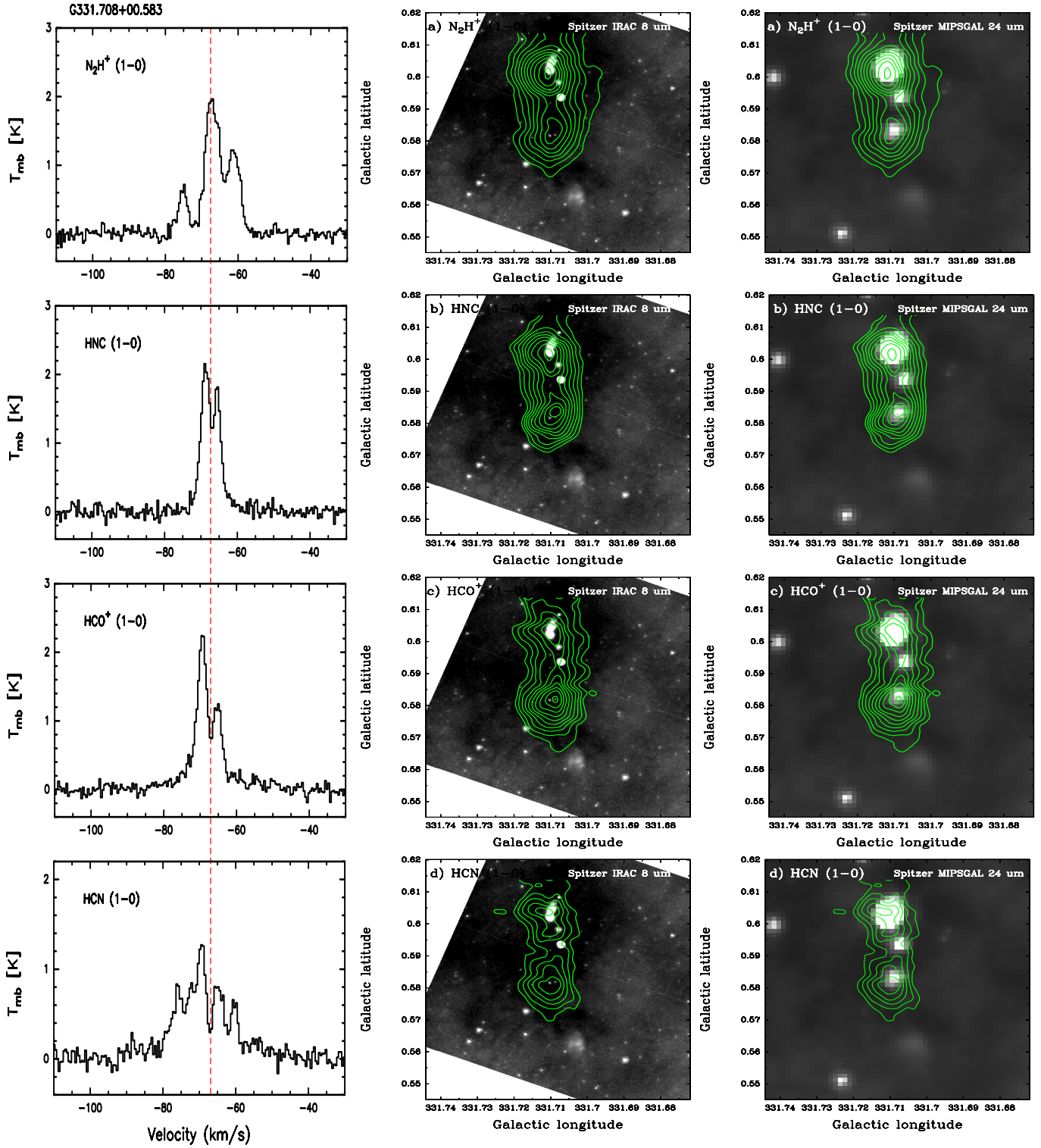


Figure 9. The spectra and the integrated intensity maps of N_2H^+ , HNC, HCO^+ , and HCN in IRDC G331.708+00.583. The spectra are in the left; the grayscale in the middle plane is *Spitzer* IRAC 8 μm and that in the right plane is *Spitzer* MIPS GAL 24 μm . The red dash line represents the V_{LSR} of N_2H^+ line

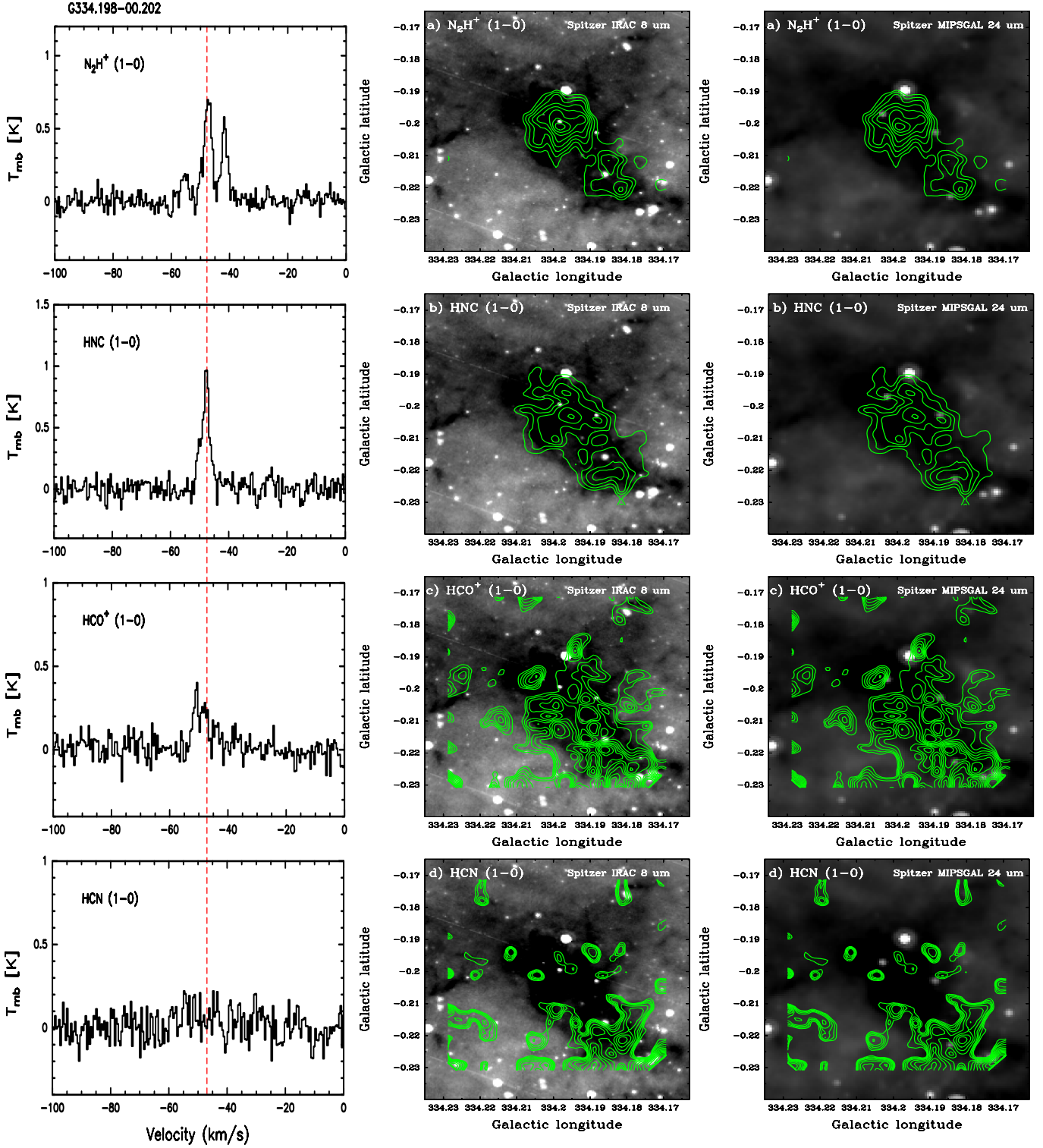


Figure 10. The spectra and the integrated intensity maps of N_2H^+ , HNC, HCO^+ , and HCN in IRDC G334.198-00.202. The spectra are in the left; the grayscale in the middle plane is *Spitzer* IRAC 8 μm and that in the right plane is *Spitzer* MIPS GAL 24 μm . The red dash line represents the V_{LSR} of N_2H^+ line

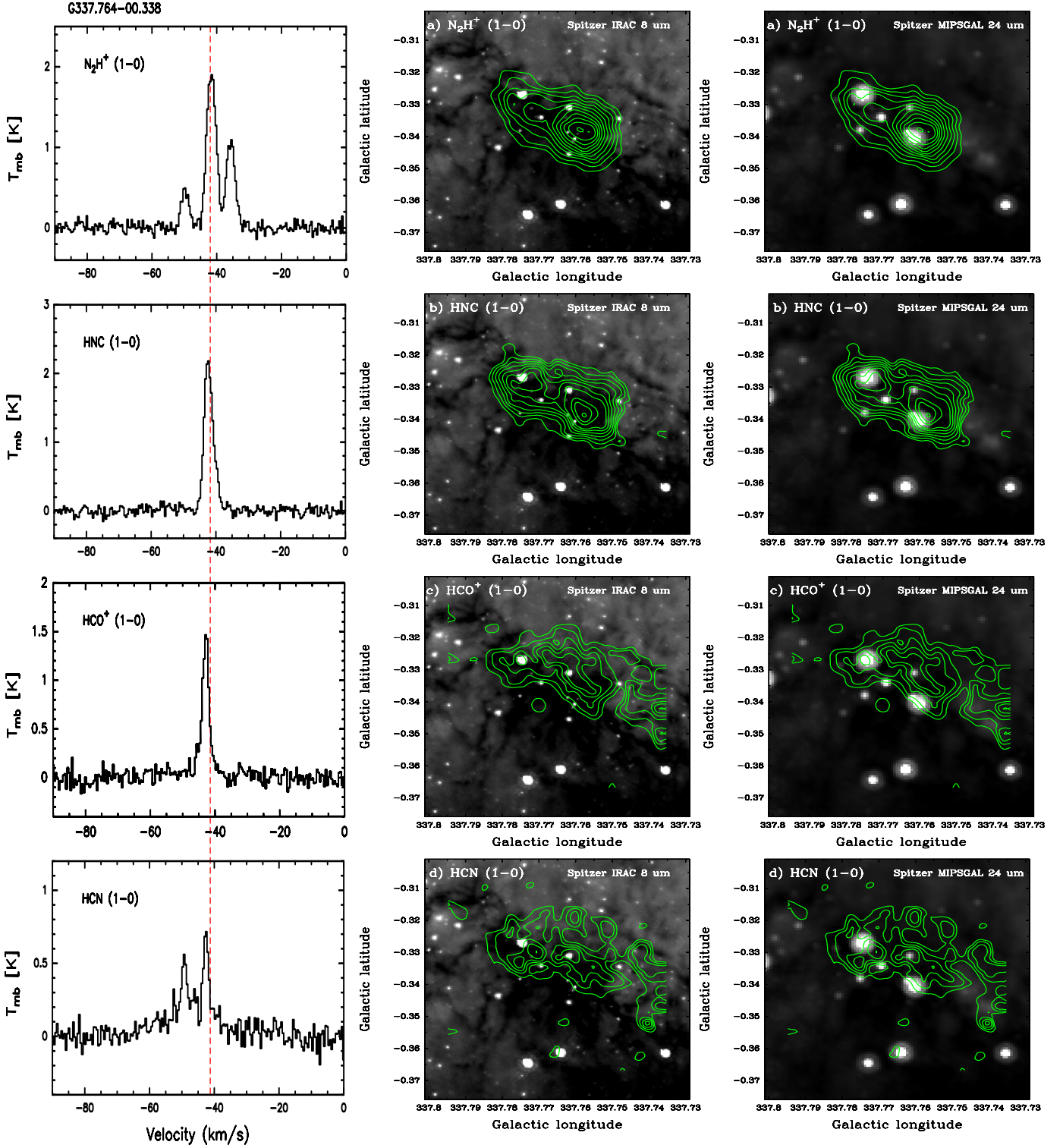


Figure 11. The spectra and the integrated intensity maps of N_2H^+ , HNC, HCO^+ , and HCN in IRDC G337.764+00.338. The spectra are in the left; the grayscale in the middle plane is *Spitzer* IRAC 8 μm and that in the right plane is *Spitzer* MIPS GAL 24 μm . The red dash line represents the V_{LSR} of N_2H^+ line

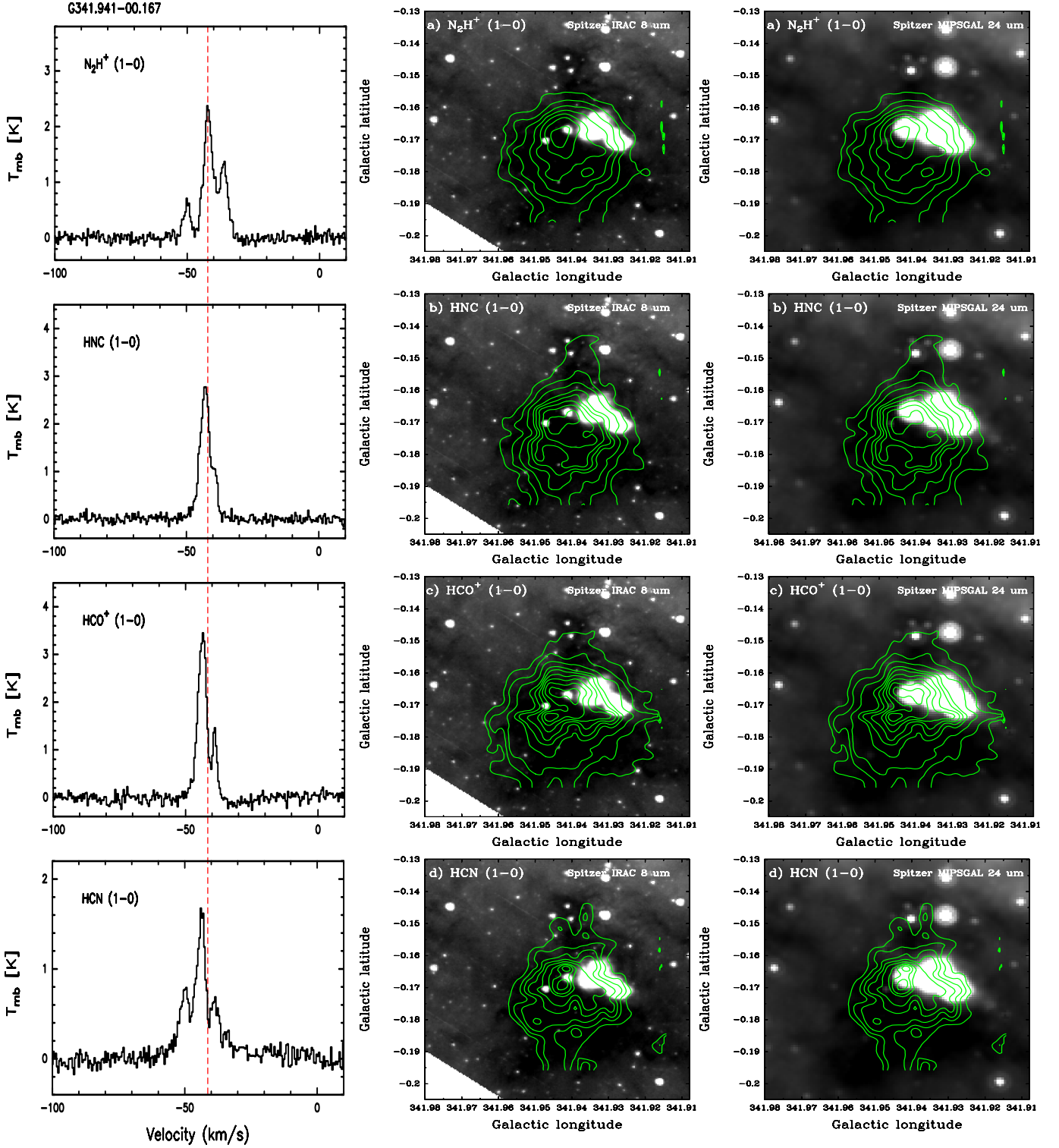


Figure 12. The spectra and the integrated intensity maps of N_2H^+ , HNC, HCO^+ , and HCN in IRDC G341.942-00.167. The spectra are in the left; the grayscale in the middle plane is *Spitzer* IRAC 8 μm and that in the right plane is *Spitzer* MIPS GAL 24 μm . The red dash line represents the V_{LSR} of N_2H^+ line

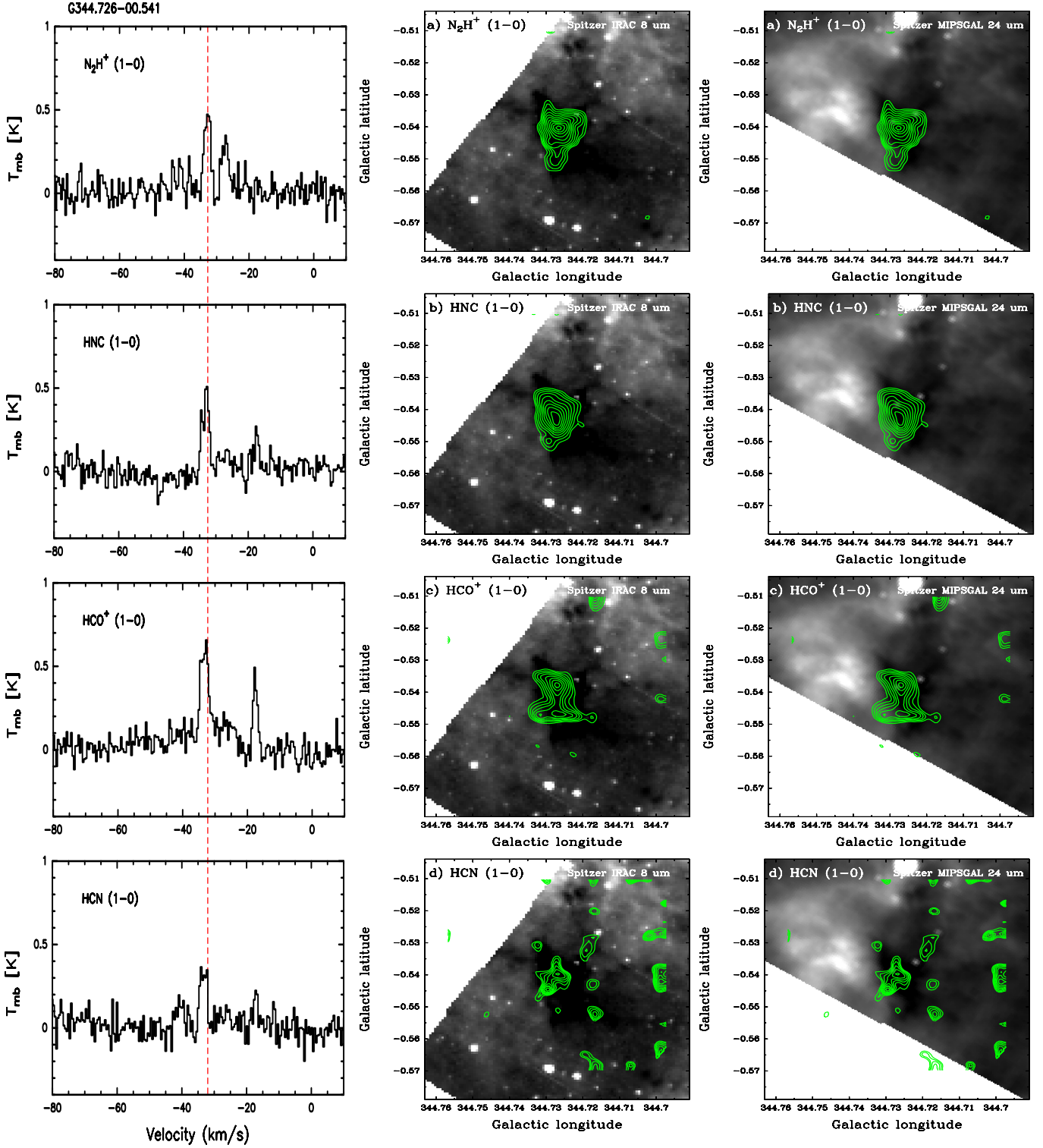


Figure 13. The spectra and the integrated intensity maps of N_2H^+ , HNC, HCO^+ , and HCN in IRDC G344.726-00.541. The spectra are in the left; the grayscale in the middle plane is *Spitzer IRAC* $8 \mu\text{m}$ and that in the right plane is *Spitzer MIPS GAL* $24 \mu\text{m}$. The red dash line represents the V_{LSR} of N_2H^+ line

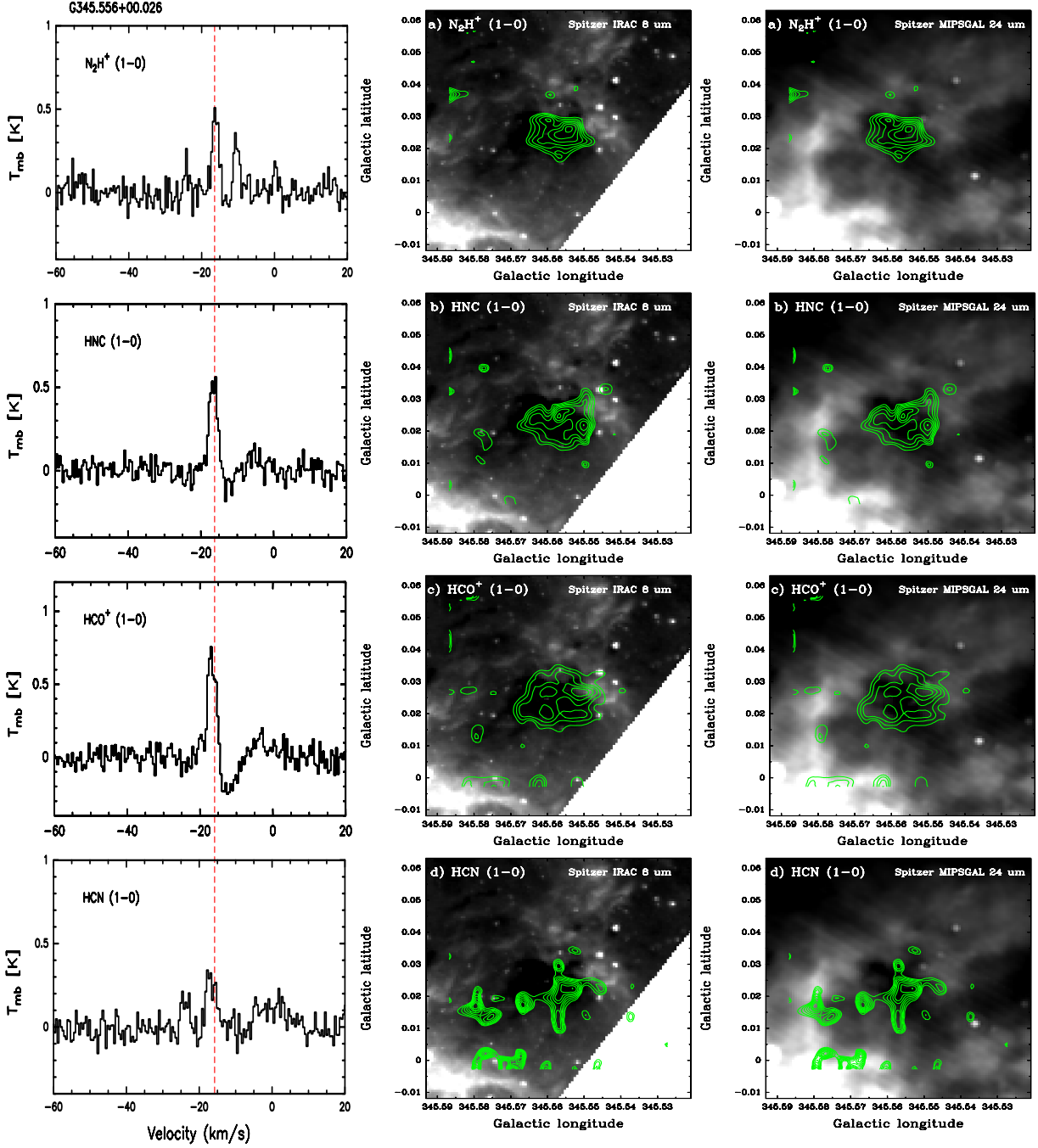


Figure 14. The spectra and the integrated intensity maps of N_2H^+ , HNC, HCO^+ , and HCN in IRDC G345.556+00.026. The spectra are in the left; the grayscale in the middle plane is *Spitzer* IRAC 8 μm and that in the right plane is *Spitzer* MIPS GAL 24 μm . The red dash line represents the V_{LSR} of N_2H^+ line

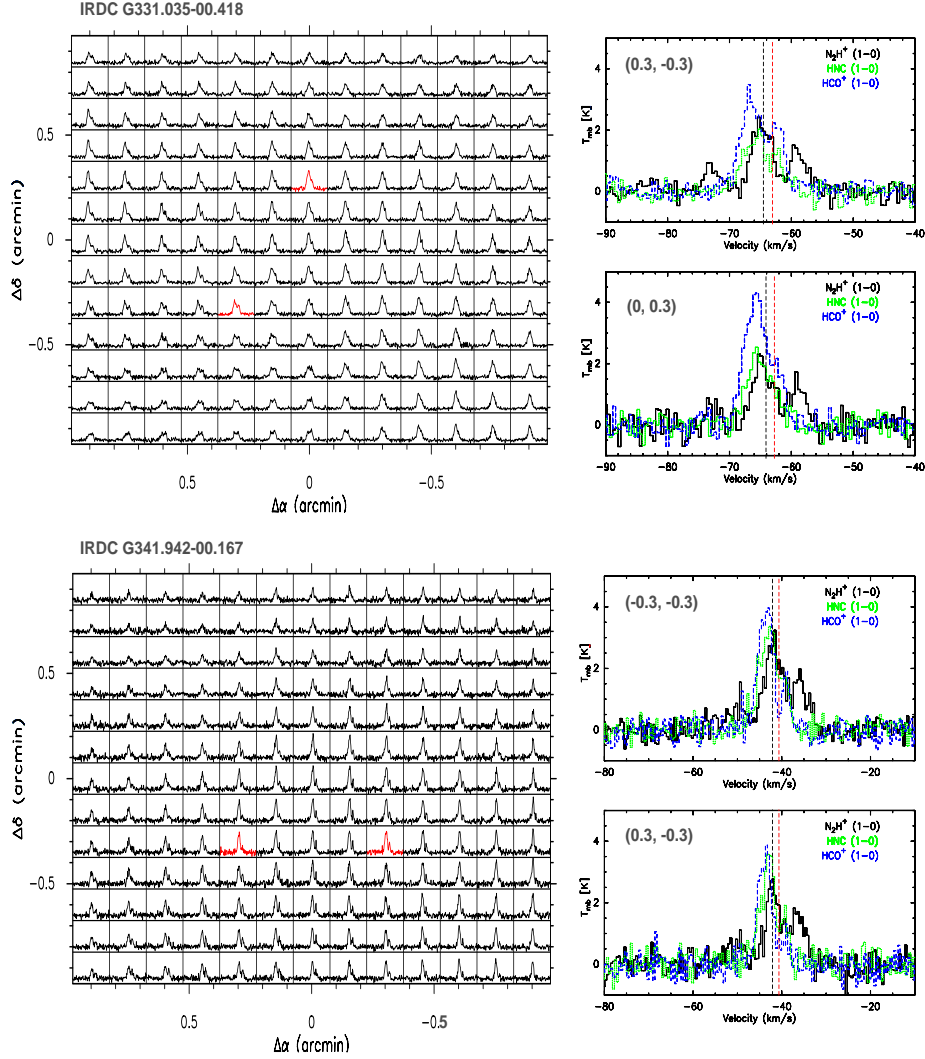


Figure 15. The upper plane: the HCO^+ map grid of *IRDC* G331.035-00.418 and the extracted spectra of N_2H^+ (black), HNC (green) and HCO^+ (blue) lines in two positions, corresponding to the red lines in the map grid. The black dash line and the red dash line mark the position of the V_{LSR} of N_2H^+ line and the absorption dip of the optically thick lines; The bottom plan: the HCO^+ map grid of *IRDC* G341.942-00.167 and the extracted spectra of N_2H^+ (black), HNC (green) and HCO^+ (blue) lines in two positions, corresponding to the red lines in the map grid. The black dash line and the red dash line mark the position of the V_{LSR} of N_2H^+ line and the absorption dip of the optically thick lines.

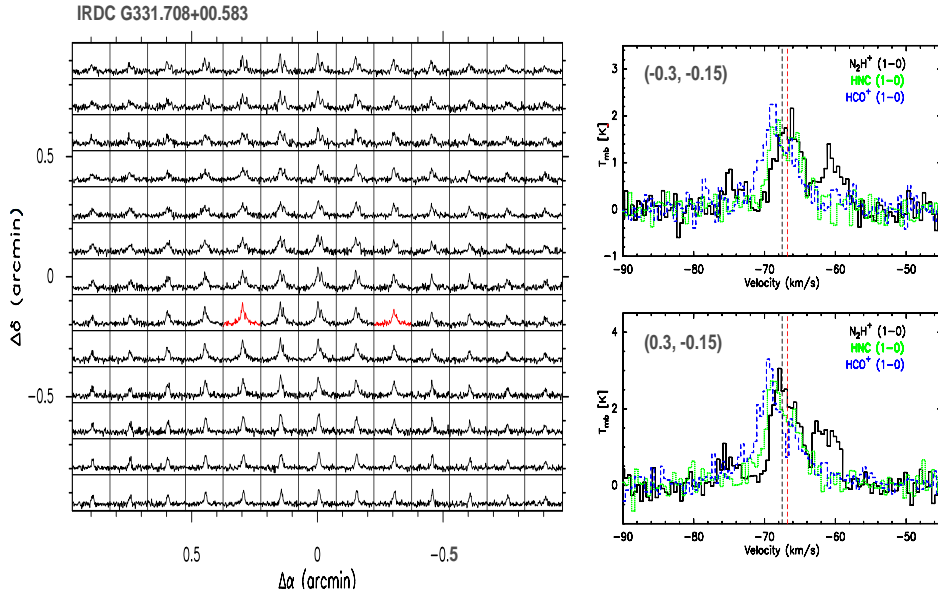


Figure 16. the HCO^+ map grid of *IRDC* G331.708+00.583 and the extracted spectra of N_2H^+ (black), HNC (green) and HCO^+ (blue) lines in two positions, corresponding to the red lines in the map grid. The black dash line and the red dash line mark the position of the V_{LSR} of N_2H^+ line and the absorption dip of the optically thick lines.

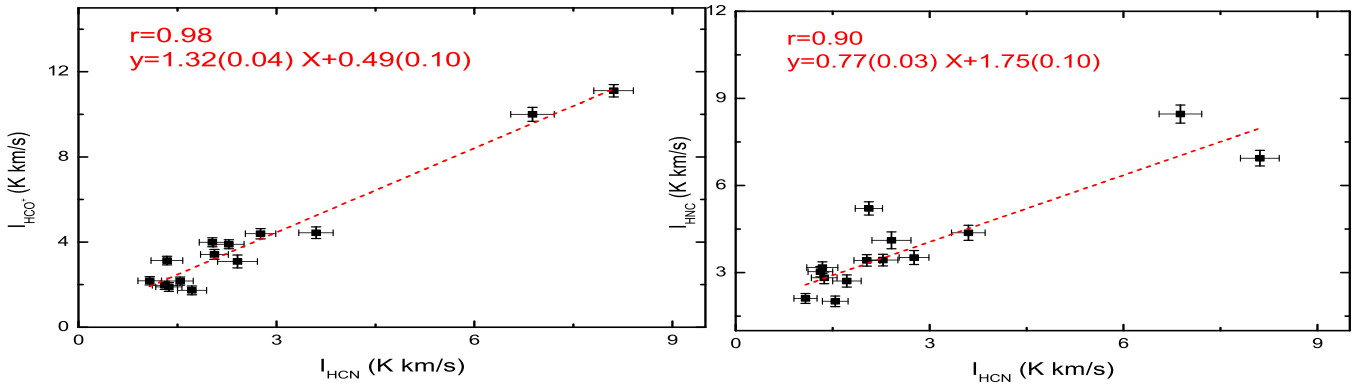


Figure 17. Left: plot averaged integrated intensity of HCO^+ vs. those of HCN for the 14 *IRDC*s. Right: same for HNC vs. HCN. The red dash lines represent the linear fitting results.

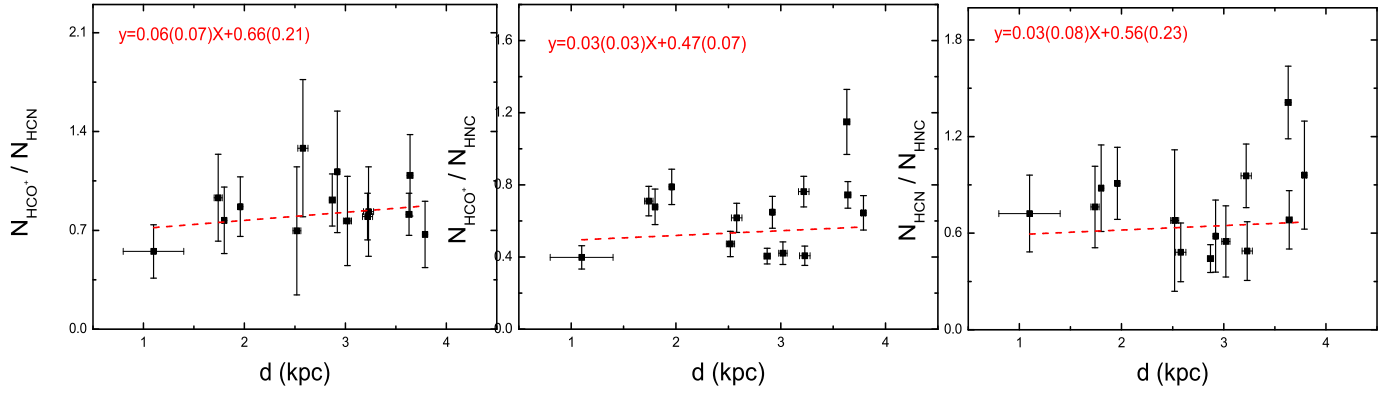


Figure 18. Left: plot average abundance ratios of HCO^+ to HCN vs. the distances of the 14 *IRDCs*. Middle: plot average abundance ratios of HCO^+ to HNC vs. the distances of the 14 *IRDCs*. Right: plot average abundance ratios of HCN to HNC vs. the distances of the 14 *IRDCs*. The red dash lines represent the linear fitting results.